UCLA
UCLA Electronic Theses and Dissertations

Title
Design and Optimization of Active Microarchitectured Metamaterials

Permalink
https://escholarship.org/uc/item/1m34t9ns

Author
Song, Yuanping

Publication Date
2018

Peer reviewed|Thesis/dissertation

eScholarship.org Powered by the California Digital Library
University of California

UNIVERSITY OF CALIFORNIA

Los Angeles

Design and Optimization of Active Microarchitectured Metamaterials

A dissertation submitted in partial satisfaction of the requirements for the degree Doctor of Philosophy in Mechanical Engineering

by

Yuanping Song

2018

© Copyright by

Yuanping Song

2018

ABSTRACT OF THE DISSERTATION

Design and Optimization of Active Microarchitectured Metamaterials

by

Yuanping Song

Doctor of Philosophy in Mechanical Engineering

University of California, Los Angeles, 2018

Professor Jonathan Hopkins, Chair

A metamaterial is a material engineered to have a property that is not found in nature. Many different types of metamaterials have been widely researched across a variety of fields. The materials are usually constructed from a repeating pattern of unit cells, whose behavior is largely driven by the design of the mechanical structure and geometry configuration. In recent years, the advancements in micro-fabrication and micro-manipulation technologies, especially in micro-additive manufacturing technologies, provide new possibilities for the fabrication of metamaterial microstructure with embedded actuators and sensors. Unlike most existing microarchitectured metamaterials that exhibit their properties based solely on their microstructure's topology and constituent material properties, active microarchitectured metamaterials exhibit the desired

behavior through the incorporated actuators. In addition to producing the desired material properties accurately, active microarchitectured metamaterials are also capable of real-time tuning and arbitrary control of such properties, providing more flexibilities for the application of metamaterials.

This research aims to provide general design guidelines for active microarchitectured metamaterials. The dissertation begins by reviewing the main methods for designing microstructure's topologies based on compliant micro-mechanisms. This is followed by a discussion of the microstructure's actuation design principles, including the optimal placement of actuators and the selection of micro-actuation physics. A numerical computational tool is then introduced that identifies the boundaries of the performance capabilities achieved by a specific design topology and generates the parameters that produce the optimal design instantiations. Examples of active microarchitectured metamaterial design are introduced and optimized to demonstrate such design principles.

The dissertation of Yuanping Song is approved.

Robert N. Candler

Jason L. Speyer

Tsu-Chin Tsao

Jonathan Hopkins, Committee Chair

University of California, Los Angeles

2018

Dedicated to Mom and Dad.

Table of Contents

List of Figures ..... **viii**

List of Tables ..... **x**

Acknowledgments ..... **xi**

Vita ..... **xiii**

Chapter 1: Introduction **1**

1.1 Overview 3

1.2 Applications 4

Chapter 2: Active Microarchitecture Design **6**

2.1 Complaint Micro-mechanism Design Methods Review 7

2.2 Optimal Actuation of Flexure Systems 9

2.2.1 Flexure system actuation 9

2.2.2 Fundamental Principles 12

2.2.3 Actuation Spaces on Intermediate Bodies 18

2.2.4 Calculating Actuation Spaces 20

2.3 Micro-actuators Actuation Physics 24

2.3.1 Actuation Types 24

2.3.2 Performance Comparison of Actuation Physics 30

Chapter 3: Optimization of Active Microarchitecture Design **33**

3.1 Introduction 33

3.2 Performance Boundary Identification 35

Chapter 4: Active Microarchitectured Metamaterial Designs **48**

4.1 A Piezo-actuated Microarchitectured Material 48
4.1.1 Design 48
4.1.2 Modeling and Optimization 52
4.2 An Electrothermal-actuated Microarchitectured Material 63
4.2.1 Design 63
4.2.2 Modeling and Optimization 68
Chapter 5: Conclusion 72
5.1 Recommended Future Work 72
Appendix A: MMA Performance Metrics 74
Appendix B: Actuator Energy Density Limits 82
Bibliography 94

List of Figures

Figure 1: Three categories of flexure systems 8
Figure 2: Static (A) and dynamic (B) actuation space 11
Figure 3: Flexure system (A), its mode shapes (B) 13
Figure 4: System DOFs (A), static actuation space on body 1 (B), actuation space at different speeds (C), force (D) and moment (E) to drive stage, dynamic actuation space (F), actuators (G) 15
Figure 5: System DOFs (A), static actuation space on body 2 (B), actuation space at different Speeds (C), force (D) and moment (E) to drive stage, dynamic actuation space (F), actuators (G) 19
Figure 6: Parameters for constructing matrix [*M*] 21
Figure 7: Analog-actuation 2D TT and TTP MMAs with actuator limits: angular energy density vs. rotational range (A); angular energy density vs. pitch (B). 31
Figure 8: Progression of the SQP and then ALPS optimization algorithms for θ=0 initialized in the objective function in the input space (A) and in the corresponding output space (B); continued progression of the same optimization algorithms for θ=$\Delta\theta$ incremented in the objective function in the same input space (C) and in the same output space (D) 41
Figure 9: Generated output dots (A); convex boundary first identified (B); new objective function minimized to identify other output dots within circular or elliptical regions (C); elliptical contour diagram of the new objective function with R=2 (D); boundary updated with a new h_{max} value (E); process successfully identifies boundaries that are concave (F) 44
Figure 10: Active microarchitectured material lattice design (A), its cell's repeated sector (B and C), a cross-section of the sector (D), and a cross-section of the unit cell (E) 49
Figure 11: Simplified unit cell topology defined by five independent parameters (A), maximum positive vs. negative strains for every design instantiation (B), maximum tensile vs. compressive forces (C), maximum strain vs. force ranges (D), maximum strain vs. force ranges result generated using the computational optimization tool introduced in Chapter 3 (E) 54

Figure 12: A general beam element with labeled parameters and coordinate axes that establish this paper's mathematical convention (A), and a cross-section of the beam element showing the nine locations at which the Mises stress is calculated at its top and bottom ends to determine if the deformed beam has yielded (B). 57
Figure 13: Active microarchitectured material lattice design (A), the center cube exposed by removing the actuators on three sides (B), the electrothermal actuator design (C) and (D)..... 64
Figure 14: Electrothermal actuator's device layer (A), handle and buried oxide layer (B), silicon nitride insulation layer (C), and gold and polysilicon layer (D) 66
Figure 15: Electrothermal actuator microfabrication process flow 67
Figure 16: Photo of the fabricated electrothermal actuator (A), SOI wafer before and after microfabrication (B)..... 68
Figure 17: Simplified thermal actuator design topology defined by eleven independent parameters 69
Figure 18: Maximum strain vs. force ranges result generated using the computational optimization tool introduced in Chapter 3 71

List of Tables

Table 1: Finite element verification of the analytical predictions pertaining to design 1 from Figure 11E with P=0.190mm, Q=0.090mm, H=0.310mm, e=0.011mm, and U=0.290mm 62
Table 2: Finite element verification of the analytical predictions pertaining to design 2 from Figure 11E with P=0.120mm, Q=0.040mm, H=0.420mm, e=0.004mm, and U=0.470mm 62
Table 3: Design parameters and their range 70
Table 4: FEA Material Properties 70

Acknowledgments

This work was supported by the UCLA Mechanical and Aerospace Engineering Departmental Fellowship, the Air Force Office of Science Research under award number FA9550-15-1-0321, and by Lawrence Livermore National Laboratory under the auspices of the U.S. Department of Energy under contract DE-AC52-07NA27344.

Section 2.2 contains the work: Hopkins, J. B., Song, Y., Wang, S., Behbahani, A. H., and Josefson, I., 2014, "Optimal Actuation of Dynamically Driven Serial and Hybrid Flexure Systems," *Volume 5A: 38th Mechanisms and Robotics Conference*, ASME, p. V05AT08A043. JH wrote the manuscript. YS et al. revised the manuscript.

Section 2.3 contains Section 5 in: Song, Y., Panas, R. M., and Hopkins, J. B., 2018, "A Review of Micromirror Arrays," Precis. Eng., **51**(August 2017), pp. 729–761. YS wrote the manuscript. JH et al. revised the manuscript.

Chapter 3 contains Section 3 in: Song, Y., Hatamizadeh, A., and Hopkins, J. B., "Optimizing the Geometry of Flexure System Topologies Using the Boundary Learning Optimization Tool," Math. Probl. Eng., **2018**. YS and AH wrote the manuscript. JH revised the manuscript.

Section 4.1 contains the work: Song, Y., Dohm, P. C., Haghpanah, B., Vaziri, A., and Hopkins, J. B., 2016, "An Active Microarchitectured Material That Utilizes Piezo Actuators to Achieve Programmable Properties," Adv. Eng. Mater., **18**(7), pp. 1113–1117. YS wrote the manuscript. PD et al. revised the manuscript.

Section 4.2 contains the work: Song, Y., Zhao, C., Ladner, I. S., Cullinan, M. A., and Hopkins, J. B, "An Active Microarchitectured Material That Utilizes Electrothermal Actuators to Achieve Programmable Properties," (in preparation). YS wrote the manuscript. CZ et al. revised the manuscript.

Appendixes A and **B** are adapted from Section 3 and Section 6 in: Song, Y., Panas, R. M., and Hopkins, J. B., 2018, "A Review of Micromirror Arrays," Precis. Eng., **51**(August 2017), pp. 729–761.

Vita

EDUCATION

MS, Mechanical Engineering Dec 2013

University of California, Los Angeles (UCLA)

BS, Mechanical Engineering June 2012

Shanghai Jiao Tong University(SJTU)

RESEARCH EXPERIENCE

Visiting Scholar – Lawrence Livermore National Laboratory July 2017 - Present

Design of a Material Logic System

- Develop a functionally complete set of mechanical logic gates that can be interconnected to form a mechanical computation system inside smart materials

Research Assistant – Flexible Research Group, UCLA Jan 2014 - Present

Parametric Optimization of Mechanical Designs (June 2016 – June 2017)

- Developed a new computational tool for optimizing the parameters of a system (typically a mechanical design) in order to achieve the optimal combinations of performance capabilities

Review of Existing Micromirror Array (MMA) Devices and Technologies (Jan 2015 – Apr 2017)

- Reviewed 277 MMA designs from 2,631 MMA research papers and patents
- Defined the basic methods of MMA classification and evaluation
- Derived the theoretical performance limits of MMAs based on different actuator designs
- Provided general guidelines for MMA designs.

Design and Control of a High Fill-factor High-speed Large-range Tip-tilt-piston Micromirror Array (Jan 2015 – Sep 2016)

- Designed a hexagonal micromirror array that is capable of independent mirror motion of three degrees of freedom (tip, tilt and piston) based on a technique using comb drives for simultaneous actuation and sensing

Design of Programmable Microarchitectured Materials (Jan 2014 – Present)

- Developed a compliant micro-mechanism based on electrothermal micro-actuators and piezoresistive polysilicon strain gauges (Apr 2016 – June 2017)
- Developed an active cubic microstructure based on piezoelectric micro-actuators and capacitive displacement sensors (Jan 2014 – Mar 2016)

PUBLICATIONS AND PATENTS

Journal Publications

[7] **Song, Y.,** Panas, R. M., Chizari, S., Shaw, L. A., Hopkins, J. B., Mancini, J. A., Pascall, A. J., 2018, "Mechanical Logic Based on Additively Manufacturable Micro-Mechanical Logic Gates," Advanced Materials, submitted.

[6] **Song, Y.**, Hatamizadeh, A., Hopkins, J.B., 2017, "Optimizing the Geometry of Flexure System Topologies Using the Boundary Learning Optimization Tool (BLOT)", Mathematical Problems in Engineering, 2018.

[5] Shaw, L.A., Dotson, M., Chizari, S, **Song, Y.**, Hopkins, J.B., 2017, "Compliant Rolling-contact Architectured Materials," Advanced Materials, submitted.

[4] **Song, Y.**, Panas, R.M., Hopkins, J.B., 2017, "A Review of Micromirror Arrays," Precision Engineering, 2017.

[3] Hopkins, J.B., Panas, R.M., **Song, Y.,** White, C.D., 2017, "A High-speed Large-range Tip-tilt-piston Micromirror Array," Journal of Microelectromechanical Systems, 26(1): pp. 196-205.

[2] **Song, Y.**, Dohm, P.C., Haghpanah, B., Vaziri, A., Hopkins, J.B., 2016, "An Active Microarchitectured Material that Utilizes Piezo Actuators to Achieve Programmable Properties," Advanced Engineering Materials, 18(7): pp. 1113-1117

[1] Hopkins, J.B., **Song, Y.**, Lee, H., Fang, N.X., Spadaccini, C.M., 2016, "Polytope Sector-based Synthesis and Analysis of Microstructural Architectures with Tunable Thermal Conductivity and Expansion," Journal of Mechanical Design, 138(5): pp. 051401-051410.

Conference Proceedings

[5] Zhao, C., Ladner, I.S., **Song, Y.**, Hopkins, J.B., Cullinan, M.A., "Design and Modeling of a Bidirectional MEMS Thermal Actuator," Proc. of the 32nd Annual Meeting of the ASPE, 2017.

[4] **Song, Y.**, Hatamizadeh, A., Hopkins, J.B., "Geometry Optimization of Flexure System Topologies Using the Boundary Learning Optimization Tool (BLOT)," Proc. of the ASME International Design Engineering Technical Conferences and Computers and Information in Engineering Conference (IDETC/CIE), 2017.

[3] **Song, Y.**, Panas, R.M., Hopkins, J.B., "Micro-mirror Array: Classification, Review, and Performance Comparison," Proc. of the 31st Annual Meeting of the ASPE, 2016.

[2] Hopkins, J.B., Panas, R.M., **Song, Y.**, "Categorization and Review of Existing Micro-mirror Array Technologies," Proc. of the 30th Annual Meeting of the ASPE, 2015.

[1] Hopkins, J.B., **Song, Y.**, Wang, S., Behbahani, A.H., Josefson, I., "Optimal Actuation of Dynamically Driven Serial and Hybrid Flexure Systems," Proc. of the ASME 2014 International Design Engineering Technical Conferences & Computers and Information in Engineering Conference IDETC/CIE, 2014.

Patents

[2] Hopkins, J.B., Hatamizadeh, A., and **Song, Y.** "Apparatus and Method for Boundary Learning Optimization", U.S. Patent Application 62/534,820, filed.

[1] Hopkins, J.B., and **Song, Y.** "Actively controlled microarchitectures with programmable bulk material properties." U.S. Patent Application 15/379,311, published.

Chapter 1:

Introduction

Researchers have created many artificial materials that exhibit better performance in specific application scenarios, such as polymers, composite materials, nanomaterials, etc. In the past ten years, the rapid development of the micro-additive manufacturing technology has enabled the fabrication of microstructures with complex geometry, which prompted the creation of a new type of artificial material — microarchitectured metamaterials [1]. Metamaterials are broadly defined as materials that exhibit properties not found in natural materials. The prefix “meta” comes from Greek meaning “beyond” or “change.” Typically, metamaterials are comprised of a periodic pattern of unit cells with rationally architectured microstructures. The unit cells are designed at scales that are smaller than the phenomena they influence, and thus collectively behave as a uniform material under a specific stimulation, such as electromagnetic wave [2], acoustic wave [3], temperature change [4], mechanical pressure [5], etc. These desired material properties are generated from the geometry configuration of each unit cell’s microstructure and thus require no chemical or atomic alterations.

Newly emerging multi-material micro-additive manufacturing [6] and micro-manipulation [7] technologies have further extended the flexibility of metamaterial microarchitecture design, allowing micro-actuators, sensors and even processors to be embedded within each cell. Such components can either be built simultaneously with the microstructure in a multi-material micro-additive manufacturing process or assembled at the designated location during the fabrication of

the microstructure. Unlike the passive microarchitectured materials that achieve the desired properties based solely on their microstructure's topology and constituent material properties, such active microarchitectured metamaterials achieve their properties primarily from the internal actuators, which are driven according to the control instructions provided by the built-in microprocessors. Moreover, if the designers wish to achieve different material properties, they do not need to redesign or refabricate the mechanical infrastructure of their initial design, but can simply reprogram and upload new control instructions to the existing design such that the different combinations of material properties can be achieved. And, since such control instructions can be altered and uploaded in real-time by connecting to a centralized master controller, desired combinations of properties can be actively and continuously tuned or maintained over appreciable ranges on demand. Active microarchitectured metamaterials can also achieve extreme properties that are theoretically unachievable by naturally occurring materials, composites, or other passive microarchitectured materials because active metamaterials are energized by a power source (e.g., batteries or an external power line) that can significantly amplify the material's response to external stimulations.

In this dissertation, a design paradigm of active microarchitectured metamaterials is introduced. In the remainder of Chapter I, an overview of the active microarchitectured metamaterials is provided, followed by a discussion of their applications. In Chapter II, we first provide a brief review of the compliant mechanism design methods. Then, the theory that guides the designers to find optimal actuator placement is introduced which is an extension of the Freedom, Actuation, and Constraint Topologies (FACT) synthesis approach [8]. The types of possible actuation physics are then analyzed and compared, which concludes Chapter II. In

Chapter III, a computational tool is introduced that identifies the boundaries of the performance capabilities achieved by an active metamaterial design topology and generates the parameters for the optimal designs. In Chapter IV, a piezo-actuated microarchitectured metamaterial and a thermally actuated microarchitectured metamaterial are introduced to demonstrate the proposed design paradigm. Chapter V summarizes the main contributions of the research and provides a discussion of the future research directions that need to be pursued.

1.1 Overview

Metamaterials were first created at the beginning of the 21st century, and unnatural electromagnetic properties have been demonstrated [9]. These early creations of metamaterials utilize split-ring resonators [10] as the units for constructing electromagnetic metamaterials. Other electromagnetic properties such as strong artificial magnetism [11], negative relative permittivity [11], and negative relative permeability [12] have been demonstrated. Inspired by the creation of electromagnetic metamaterials, acoustic metamaterials [3,13] were developed with artificial properties associated with mechanical wave propagation. More recently, various mechanical metamaterials [1,14] were designed and fabricated that demonstrated unusual mechanical properties such as negative compressibility [15], ultrahigh stiffness-to-density ratio[16], negative Poisson's ratio [17], anisotropy [18], etc. Unique thermal properties such as tunable thermal conductivity and expansion [4] have also been achieved by microarchitectured metamaterials. By introducing active elements (that can be actuated or controlled through built-in electronic circuits or external fields such as electric and magnetic fields) into the microarchitecture of different types

of metamaterials, researchers have designed various active microarchitectured metamaterials with tunable electromagnetic [19,20], acoustic [21,22], and mechanical [23,24] properties.

The concept of metamaterial may be generalized to include metasurfaces [25] as planar metamaterials. These metasurfaces are usually designed to have unusual surface or interface properties such as anomalous wave reflection and refraction [25], wavefront shaping [25], polarization conversion [25], and superhydrophobicity [26]. Active metasurfaces have also been developed [25,27] that demonstrated controllable properties and behaviors. Such active metasurfaces are typically constructed by arranging the actuated microarchitectured units in a planar periodic pattern and therefore share very similar design principles to spatial active metamaterials.

1.2 Applications

Given the short history of active microarchitectured metamaterials, the successful demonstrations of the application of active metamaterials are very limited. Nonetheless, active metamaterials have a huge potential in various applications that extend beyond the range of the traditional passive metamaterials. Here, we categorize the applications into two main groups based on the main functions of active metamaterials — applications that utilize the morphing shapes and surfaces and applications that utilize the controllable material properties.

One of the unique advantages of active metamaterials is that they are able to actively deform into the desired shape or surface profile [28]. Morphing aircraft wings [29] made from an active metamaterial can change their shape and angle according to control instructions such that the optimal aerodynamic characteristics are achieved in varying flight conditions, which improve

aircraft maneuverability and fuel efficiency. Additionally, the precise control of active metasurfaces enables various optical applications [25,27] that requires light manipulation, such as direct optical signal switching and routing [30], novel display technologies [31], optical imperfection correction in space-based telescopes [32], advanced microscopy [33] and vision science [34].

Active metamaterials are also utilized in applications for their controllable bulk and surface properties. Active electromagnetic metamaterials [19] offer several advantages over passive electromagnetic metamaterials, such as tuning capabilities and wider working bandwidth, and thus allow for more flexibilities in applications such as optical cloaking, perfect absorbers, superlenses, etc. Active acoustic metamaterials [21] enable applications such as acoustic cloaking, vibration absorption, and wave amplification. Active mechanical metamaterials [14,24] achieve different combinations of desired mechanical properties (e.g., Young's Modulus, Poisson's ratio, density, and damping coefficient) simultaneously. Such metamaterials may be applied in various applications, such as space aircraft and equipment, soft robotics design, and artificial muscles development, to meet the specific material requirements. Active metasurfaces [25] with unit cells at the micro- and submicro-scale are able to alter their surface "textures" by individually controlling the actuation of each cell to generate the desired periodic surface pattern. Such artificial surface textures could be applied on surfaces of high-speed vehicles to adaptively reduce the friction drag. Additionally, by varying the surface textures, an active metasurface could transfer from a hydrophilic surface to a superhydrophobic surface [26].

Chapter 2:

Active Microarchitecture Design

In this Chapter, we introduce a general design methodology of active microarchitectured metamaterials. The design of an active microarchitectured material is essentially the design of the active unit cells. Each unit cell contains controllable micro-actuators incorporated within its microstructure. The unit cells are interconnected with each other in a manner such that a specific behavior can be replicated or amplified throughout the whole lattice of unit cells. The design of a unit cell is decomposed into two parts: the design of the compliant microstructure and the design of the micro-actuators.

In Section 2.1, we review the existing methods for compliant mechanism design. These design methods guide designers in synthesizing the infrastructures of the active unit cells. In Section 2.2, we introduce a theory that generates the optimal number and placement of actuators for a general flexure system. The theory established in this section is an extension of the Freedom, Actuation, and Constraint Topologies (FACT) synthesis approach. This theory helps the designers to design to determine the position of the micro-actuators within each unit cell, such that the microstructures are driven to achieve the desired DOFs with the minimal parasitic error at any desired speed. In Section 2.3, we review and compare the existing actuation physics for micro-actuation. Actuation types such as electrostatic plates, electrostatic combs, piezoelectric actuators, thermal actuators and electromagnetic actuators are introduced and analyzed based on the

underlying physics. A quantitative comparison of the actuation types is provided based on the existing micro-mirror array (MMA) devices.

2.1 Complaint Micro-mechanism Design Methods Review

Compliant flexure systems consist of rigid bodies (shown as rectangles in the schematic of Figure 1) that are joined together by compliant elements (shown as springs in the same schematic) that elastically deform to achieve the system's precise motions [35]. Flexure elements, like the wire and blade flexures shown in the 'Example' section of Figure 1, are stiff in certain directions but compliant in other directions (e.g., wire flexures are stiff along their axis but compliant in transverse directions). Thus the placement and orientation (i.e., layout or topology) of the flexure elements within a system is the primary factor that determines the system's degrees of freedom (DOFs). The DOFs of a flexure system are the motions of greatest compliance associated with the system's stage.

Researchers have proposed several methods that help the designers to synthesize a compliant mechanism topology systematically. The Pseudo-Rigid-Body Model (PRBM) [36,37] is a method first introduced by Larry. L. Howell in 1994 to aid the design of compliant mechanisms. It is a modeling technique that approximates a compliant/flexure mechanism as a traditional mechanism that consists of rigid bodies connected by rotary joints with a torsional stiffness. The PRBM theory converts the design of a compliant mechanism into the design of a classical rigid-body mechanism, and thus simplifies the process of design topology synthesis. It is especially accurate and effective for compliant mechanisms where the joints experience large deflection and exhibit non-linear behavior.

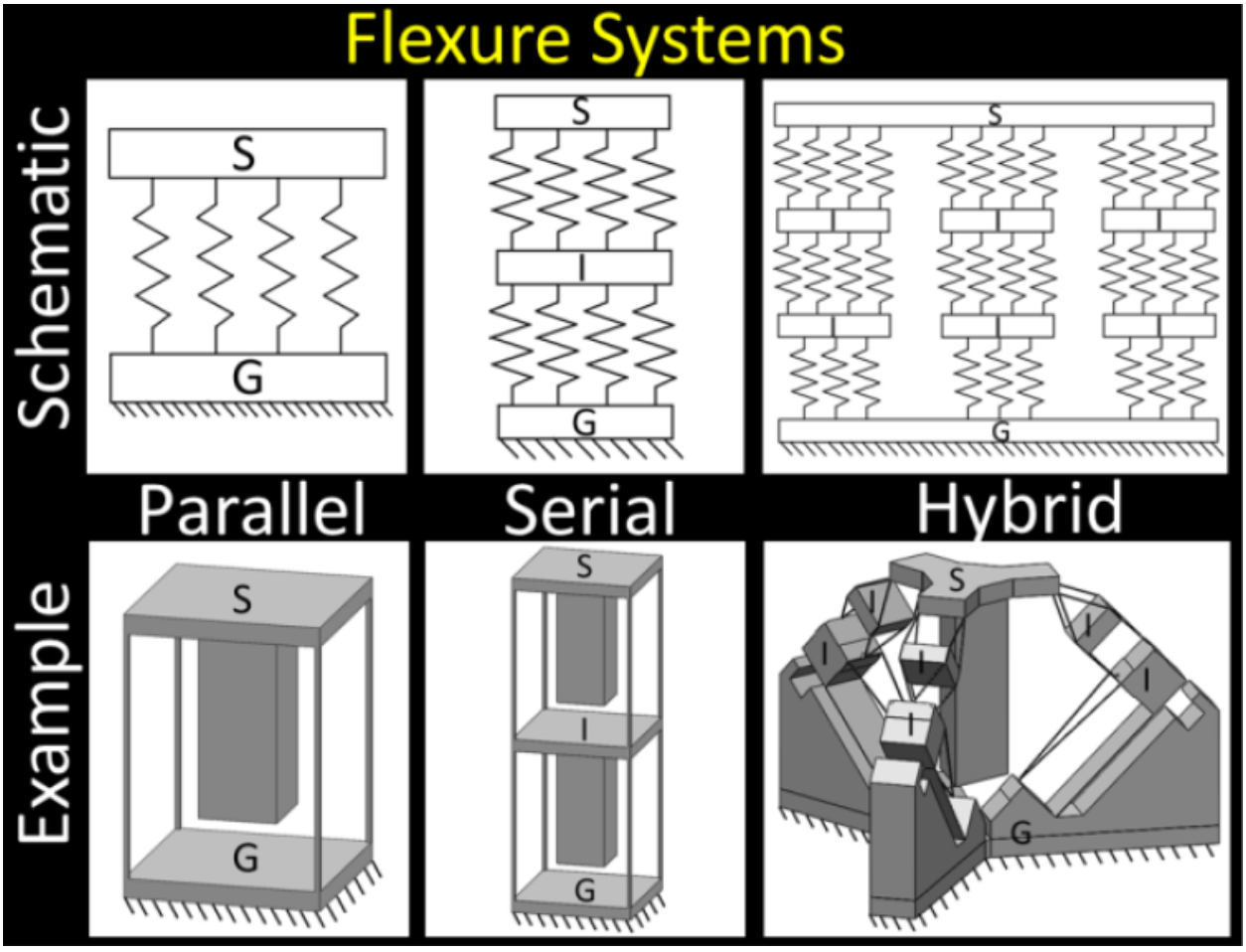

Figure 1: Three categories of flexure systems

Topology Optimization (TO) [38] is a method that models and solves the problem of distributing a limited amount of material in a design space. The TO method is widely used for the design of compliant mechanisms. This method models the design problem as a mathematical optimization problem where it optimizes a specific performance of the system for a given set of loads, boundary conditions, and constraints and generates the optimal material distribution within a given design space. It combines the utility of design topology synthesis and parametric optimization, and in

theory, generates the optimal design for any design objectives. However, solving complex design problems often requires a massive amount of calculation, and thus is impractical or unaffordable in some cases.

The freedom and constraint topologies (FACT) synthesis approach [39–41] was created to help designers rapidly consider and compare the compliant flexure topology solutions that achieve the desired set of degrees of freedom (DOFs). FACT utilizes a complete library of spaces, which provides guidelines for arranging the best number and kind of flexible elements within the geometry of the spaces for synthesizing topologies that stiffly constrain the system's bodies to not move in certain directions while permitting them to move in other directions with high compliance (i.e., the DOFs). The mathematics underlying FACT are such that only the number, kind, location, and orientation of the flexible elements that constitute the resulting topologies are considered during the synthesis process. The material properties and geometric parameters are not considered. Thus, once a design topology is synthesized, a follow-up optimization process is often required to determine the optimal design parameters.

2.2 Optimal Actuation of Flexure Systems

2.2.1 Flexure system actuation

Although a flexure system's topology is the primary factor that determines the system's DOFs, the ability to actuate the system's stage with the motions associated with the system's DOFs is not a trivial problem. There are many ways to place actuators such that they drive the stage of a well-designed flexure system with motions that come close to achieving the motions associated with the system's DOFs, but positioning actuators such that they achieve these motions exactly with no

parasitic error is often difficult and not intuitive. To make matters more complicated, the optimal actuator placement necessary to drive the DOFs of a stage change according to the speed with which the system is driven.

The most complex flexure systems to actuate are serial and hybrid systems. Unlike parallel systems that consist of a single rigid body joined directly to a fixed ground by flexure elements (Figure 1), serial and hybrid systems consist of multiple rigid bodies joined together by flexure elements of various configurations. More specifically, serial flexure systems consist of two or more parallel system modulus stacked or nested in a chain-like configuration one after the next (Figure 1). Hybrid systems consist of various combinations of parallel and serial configurations. In Figure 1, for example, the hybrid system shown consists of three serial limbs arranged in parallel. Note also from Figure 1that the fixed grounds are labeled G, the intermediate rigid bodies are labeled I, and the stages are labeled S. Even in quasi-static scenarios, actuating serial and hybrid systems is more complicated than actuating parallel systems because the final stage of a serial or hybrid system can be driven not only by loading the stage directly, but also by loading other intermediate rigid bodies that then cause the stage to move with the desired DOFs. Thus, for serial and hybrid systems, there are many more options for driving the system's stage with minimal parasitic error and the mathematics necessary to consider all of these options is significantly more complicated to formulate and manipulate than for parallel systems. Serial and hybrid systems are also more complicated to actuate when their stages are driven with appreciable speeds (i.e., dynamic scenarios). The intermediate rigid bodies within such systems introduce extra mass, which can result in complicated mode shapes and natural frequencies that can be unintentionally excited if actuation is not executed correctly.

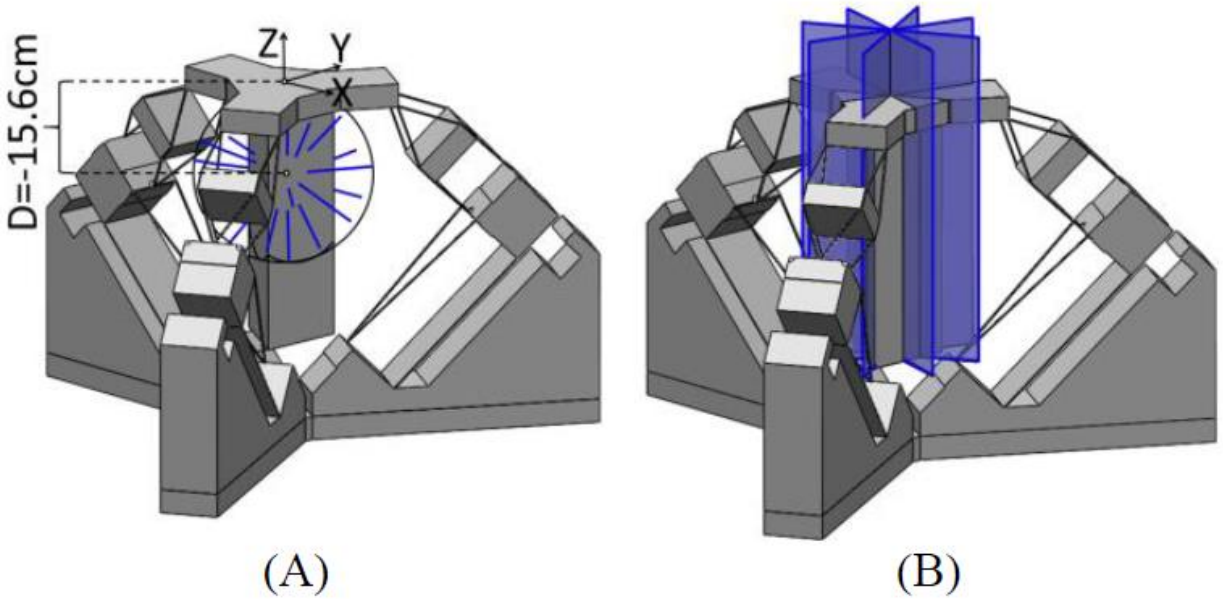

Figure 2: Static (A) and dynamic (B) actuation space

The theory presented in this section is an extension of the FACT synthesis approach, which utilizes a comprehensive body of geometric shapes to enable the rapid visualization of every flexure topology and actuation layout that successfully achieves a desired set of DOFs. The shapes that guide designers in visualizing every correct actuation layout are called actuation spaces. There are two types of actuation spaces—static and dynamic. For the hybrid system of Figure 1, its static and dynamic actuation spaces applied to the system's stage are shown in blue in Figure 2A and 2B respectively. These geometric shapes represent the regions of space within which the axes of linear actuators should be placed to drive the system's stage with the minimal parasitic error. The concept of actuation space was first introduced by Hopkins in [42] and [43] for parallel systems. In this section, we extend the mathematics underlying these spaces such that designers can actuate serial

and hybrid systems quasi-statically and dynamically. The following assumptions are made for the design of actuation. First, we assume small motion linear elasticity. We also neglect the effects of damping. And although we only provide the theory necessary to actuate flexure systems that consist of slender flexure elements that may be modeled using Bernoulli-Euler beam theory, the theory may be minimally adapted to apply to flexure elements of any geometry.

2.2.2 Fundamental Principles

This section reviews the basics of FACT's actuation approach in the context of the serial flexure system shown in Figure 3A. Its geometric parameters are labeled in the figure and its Young's modulus is 69GPa, its shear modulus is 27Gpa, and its density is 2700kg/m^3. The system consists of two identical parallel flexure system modules stacked in series. The first rigid body labeled 1 in the figure is the system's stage and the second rigid body labeled 2 is an intermediate body.

The system's first six mode shapes with their corresponding natural frequencies, ω_1 through ω_6, are provided in *(i)* through *(iv)* of Figure 3B. Note that *(i)* and *(ii)* provide mode shapes that correspond with two natural frequencies each. These two natural frequencies correspond with identically shaped modes moving in different directions (i.e., one along the *x* and the other along the *y*-axes of the coordinate system of Figure 3A). If the system is changed to a parallel system (labeled * in Figure 3B) by holding body 1 fixed with respect to the thatched ground labeled *G*, and allow body 2 to become the system's new stage, the system's first three mode shapes and their corresponding natural frequencies, ω^*_1 through ω^*_3, are shown in *(v)* and *(vi)* of Figure 3B.

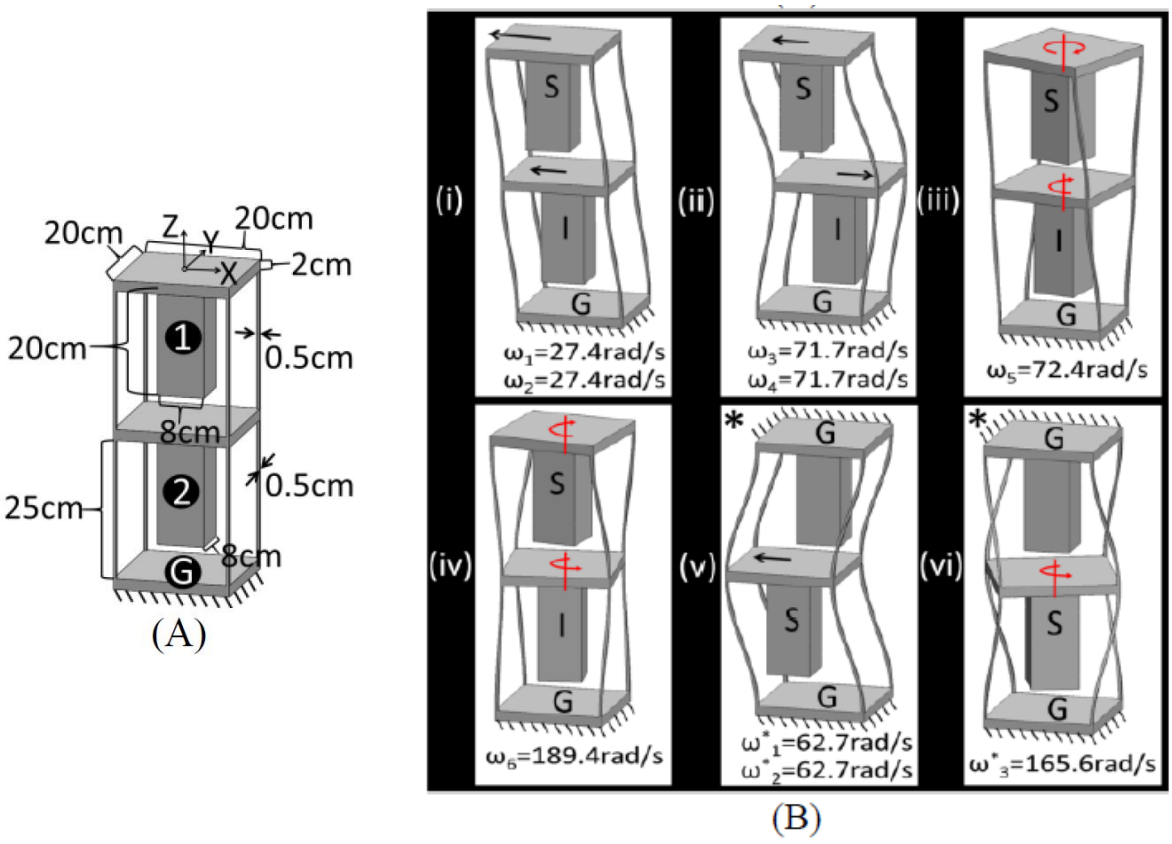

Figure 3: Flexure system (A), its mode shapes (B)

The eight slender wire flexures of the serial system allow its stage (labeled body 1 in Figure 3A) to achieve three DOFs—two translations shown as black arrows in Figure 4A, and one rotation shown as a red line with an arrow about it axis. These DOFs are modeled using twist vectors [44] and are labeled $\mathbf{T}_{j,i}$ in the figure, where *j* is the number of the labeled rigid body to which the twist applies and *i* is the labeled DOF number. Thus, the second DOF of body 1, is the black translation arrow labeled $\mathbf{T}_{1,2}$ in Figure 4A. If we wished to quasi-statically drive this stage by actuating the stage directly, there is only one correct way to do so such that the stage moves with this desired translation exactly (i.e., with no parasitic error). That correct actuation load is shown as the thick

blue arrow labeled $\mathbf{W_{1,2}}$ in Figure 4A. The blue line that passes through this arrow is modeled by the pure force wrench vector [44], $\mathbf{W_{1,2}}$, and represents the theoretically optimal actuation force acting on body 1 to drive DOF $\mathbf{T_{1,2}}$ with no parasitic error. Note, however, that this force does not pass through the stage but rather through the top portion of body 2. Thus, if we wish to actuate the stage by pushing directly on the stage such that it moves with its desired translation $\mathbf{T_{1,2}}$, we'd have to extend the stage's post as shown with the dotted lines in Figure 4A and cut a hole in the middle of body 2 to allow the stage enough clearance to push on it. The other theoretically optimal ways to actuate the other two DOFs (i.e., the translation labeled $\mathbf{T_{1,1}}$ and the rotation labeled $\mathbf{T_{1,3}}$ in Figure 4A) are modeled using wrench vectors $\mathbf{W_{1,1}}$ and $\mathbf{W_{1,3}}$ respectively. Note that $\mathbf{W_{1,3}}$ is a pure moment wrench vector and is shown as a black line with an arrow about its axis. Note also that the subscripts for wrench vectors in this paper follow a similar convention to the subscripts for twist vectors (i.e., $\mathbf{W_{k,I}}$ is an actuation load that acts on body *k* and drives the *i*th DOF labeled).

Although the stage is capable of moving with three DOFs, it may also move with every combination of these DOFs. These motions are visually depicted by the system's freedom space [8]. Freedom space is a geometric shape that represents all the ways a system may move. The freedom space of this example consists of an infinitely large box of parallel rotation lines (shown red in Figure 4B) and a disk of translation arrows that are perpendicular to these lines. If $\mathbf{T_{1,1}}$, $\mathbf{T_{1,2}}$, and $\mathbf{T_{1,3}}$ are linearly combined, this freedom space is generated. For the case of quasi-static actuation, the optimal locations and orientations of the actuators that successfully drive all the motions/twists within this freedom space also lie within a geometric shape called a static actuation space [42]. This space results from the linear combination of $\mathbf{W_{1,1}}$, $\mathbf{W_{1,2}}$, and $\mathbf{W_{1,3}}$ and consists of a plane of pure forces (shown blue in Figure 4B) and an orthogonal moment.

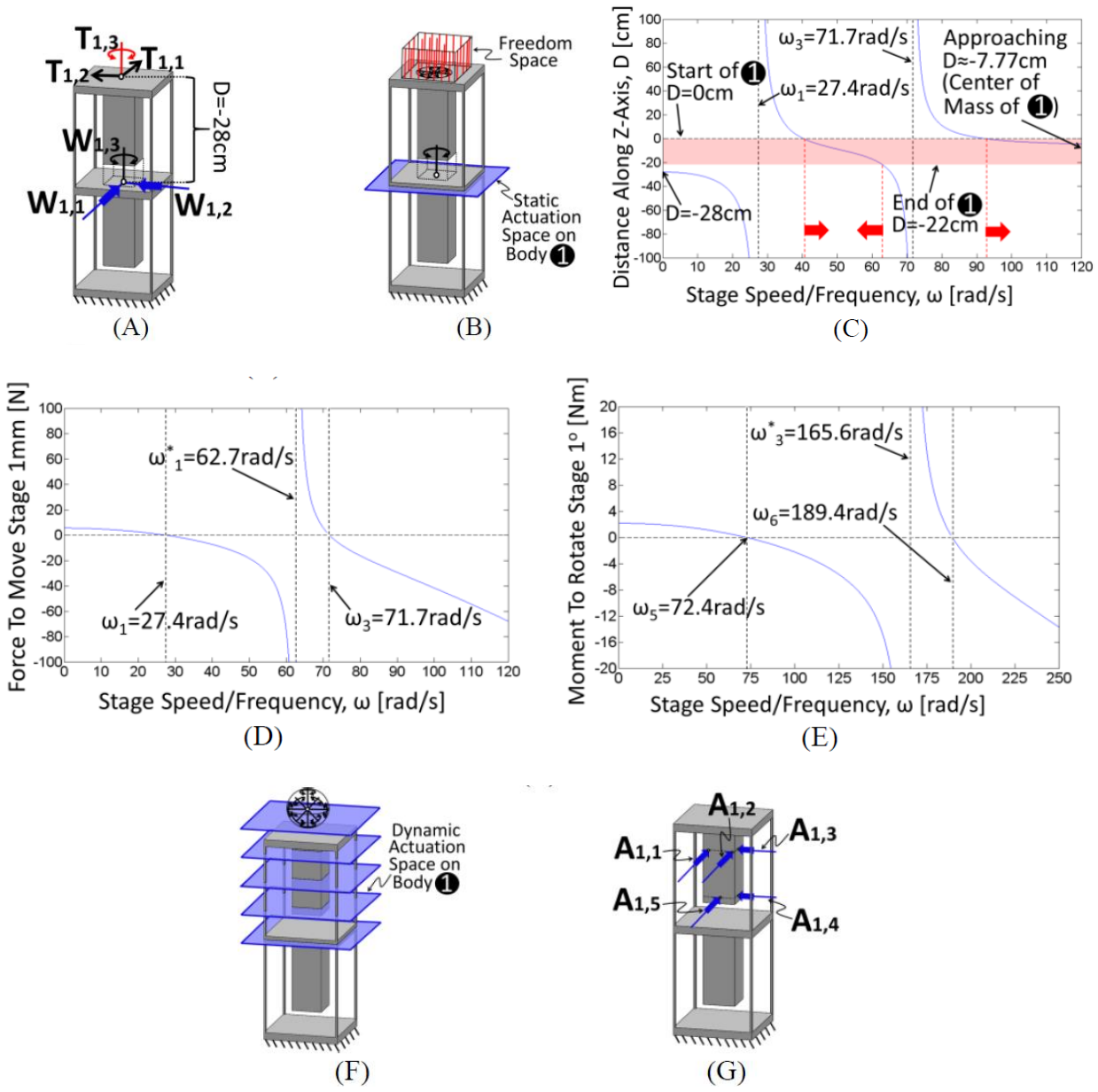

Figure 4: System DOFs (A), static actuation space on body 1 (B), actuation space at different speeds (C), force (D) and moment (E) to drive stage, dynamic actuation space (F), actuators (G)

The optimal location of this actuation space will remain at the system's center of stiffness (i.e., *D*=-28cm where *D* is the distance from the origin of the coordinate system of Figure 3A along the

z-axis) only if the DOFs in the freedom space are actuated with quasi-static speeds. If, however, we wish to actuate the motions within the freedom space with an increasing sinusoidal frequency of ω, the optimal location of the actuation space will displace downwards until it is infinitely far away when ω reaches the system's first natural frequency, ω_1 (Figure 3B) as shown in Figure 4C. As ω increases further, the planar actuation space descends from positive infinity and back down to negative infinity at the third natural frequency, ω_3. Finally, as ω increases to infinity, the planar actuation space descends from positive infinity until it approaches the stage's center of mass. The effect of increasing ω on the magnitudes of the actuation forces modeled by $\mathbf{W_{1,1}}$ and $\mathbf{W_{1,2}}$ (Figure 4A) that are necessary to displace the stage a sustained-amplitude of 1mm in the directions of $\mathbf{T_{1,1}}$ and $\mathbf{T_{1,2}}$ respectively, is shown in Figure 4D. Note that this magnitude is zero at the first and third natural frequencies, ω_1 and ω_3, and it approaches infinity at the first natural frequency of the parallel system, ω^*_1, as shown in *(v)* of Figure 3B. When the force is negative, the direction it's pushing on the stage is opposite to the direction the stage is moving (i.e., it is 180^o out-of-phase). The two rigid bodies, 1 and 2, move in the same direction with frequencies less than ω^*_1, but move in opposite directions with frequencies greater than ω^*_1. The effect of increasing ω on the magnitude of the actuation moment modeled by $\mathbf{W_{1,3}}$ (Figure 4A) that is necessary to rotate the stage a sustained-amplitude of 1^o about $\mathbf{T_{1,3}}$ is shown in Figure 4E. Note the frequencies when this magnitude is zero and when it approaches infinity and how these frequencies correspond to the mode shapes of Figure 3B.

Although the plot of Figure 4C represents the optimal location of the planar actuation space applied to body 1 for driving all the motions within the system's freedom space (Figure 4B) at any speed, only the shaded red band in Figure 4C represents the locations where the forces within the

actuation space pass through the geometry of body 1 and can thus physically actuate it. For quasi-static scenarios, the shape and mass of the rigid bodies don't affect the location of the actuation space, so the geometry of the bodies can be altered to ensure that the forces within the space do pass through the desired body (recall the dashed post shown in Figure 4A). When, however, the system is driven at finite speeds, the mass and shape of the bodies do affect the system's actuation space and can thus not be independently altered. Nonetheless, every motion within the system's freedom space can be actuated at any speed and actuators don't need to move. This can be achieved by utilizing the concept of dynamic actuation space [43]. If the wrench vectors within every planar actuation space for all values of ω are linearly combined, the stage's dynamic actuation space is generated. The dynamic actuation space of a system is a geometric shape that represents the regions of space from which all actuators can be selected that will successfully drive the motions within the system's freedom space with no parasitic error at any speed. The dynamic actuation space of the system of Figure 4F consists of an infinite number of stacked parallel planes that contain pure force wrenches (shown blue) as well as a sphere of pure moment wrenches (shown black). The dynamic actuation space also contains stacked planes of coupled moment/force wrenches, which are not shown here to avoid visual clutter. Unlike the system's planar static actuation space (Figure 4B) that contains three independent wrench vectors (like those shown in Figure 4A), the dynamic actuation space of Figure 4F contains five independent wrench vectors. Thus, while quasi-static actuation requires only three actuators selected from the plane of Figure 4B to drive the system's three DOFs with minimal parasitic error, dynamic actuation requires at least five actuators selected from the parallel planes of Figure 4F. As long as the wrench vectors that model these five actuators are all independent, like the wrench vectors labeled $\mathbf{A_{1,1}}$ through $\mathbf{A_{1,5}}$ shown in Figure 4G, their

output forces may be combined to actuate any motion within the system's freedom space with minimal parasitic error at any speed without the actuators needing to change locations. Note that the wrench vectors that model the actuators selected from within a dynamic actuation space are labeled $\mathbf{A_{t,m}}$, where the subscript *t* is the labeled number of the body on which the actuator acts and *m* is the number of the labeled actuator itself.

2.2.3 Actuation Spaces on Intermediate Bodies

Serial systems possess multiple rigid bodies and thus provide designers with multiple actuation space options for driving the system's stage with no parasitic errors. In this section we will demonstrate this principle using the example system of Figure 3 and Figure 4. This system's three DOFs, $\mathbf{T_{1,1}}$, $\mathbf{T_{1,2}}$, and $\mathbf{T_{1,3}}$, are shown in Figure 5A. Suppose now we wish to quasi-statically drive these DOFs by loading the system's intermediate body (i.e., body 2) instead of loading the system's stage directly. The two pure force loads, $\mathbf{W_{2,1}}$ and $\mathbf{W_{2,2}}$, that correctly drive $\mathbf{T_{1,1}}$ and $\mathbf{T_{1,2}}$ respectively, and the moment load, $\mathbf{W_{2,3}}$, that correctly drives $\mathbf{T_{1,3}}$ are shown in Figure 5A. By linearly combining these wrench vectors, we generate the system's static actuation space on body 2. This static actuation space is again a blue plane of pure forces and a perpendicular moment as shown in Figure 5B. If we wish to actuate the motions within the system's freedom space with an increasing sinusoidal frequency of ω, the optimal location of the actuation space will displace a distance *D* along the *z*-axis of Figure 3A according to the plot of Figure 5C. Note that as ω approaches infinity, the planar actuation space settles at the center of mass of body 2. The shaded red band in Figure 5C represents the locations at which the pure forces within the planar actuation space pass through body 2. Although the plots of Figure 5C-E are significantly different from the plots of Figure 4C-E, the dynamic actuation space on body 2 (Figure 5F) is coincidentally the same

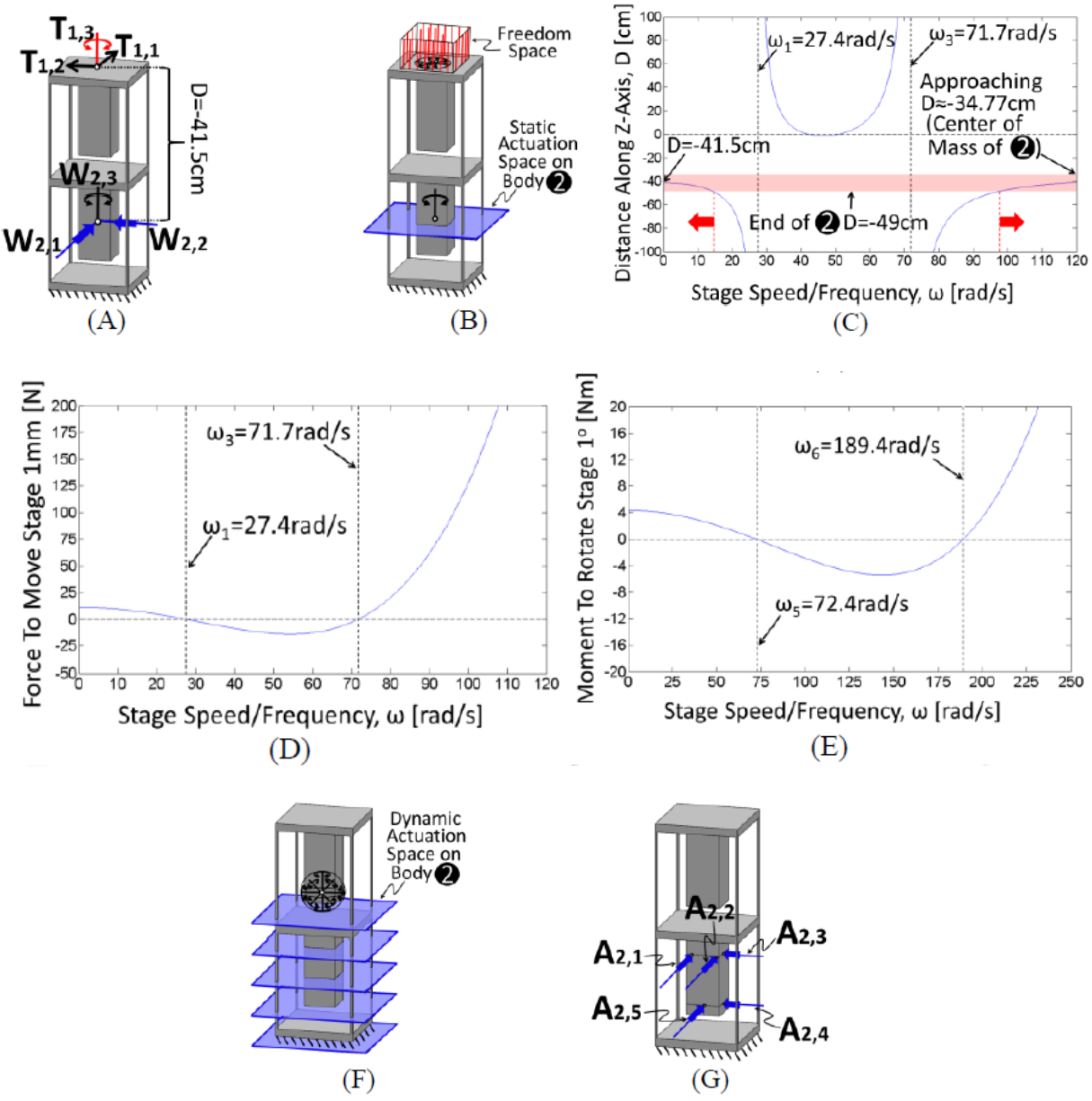

Figure 5: System DOFs (A), static actuation space on body 2 (B), actuation space at different Speeds (C), force (D) and moment (E) to drive stage, dynamic actuation space (F), actuators (G)

as the dynamic actuation space on body 1 (Figure 4F). This is not usually the case for general serial or hybrid systems, but because this system's dynamic actuation space is the same on body 2 as it is on body 1, we can select a similar set of five actuators from within the space (e.g., $\mathbf{A}_{2,1}$ through $\mathbf{A}_{2,5}$ in Figure 5G) that can correctly actuate all the system's DOFs within minimal parasitic error at any speed.

2.2.4 Calculating Actuation Spaces

In this section, we introduce the mathematics necessary to generate the static or dynamic actuation space acting on any desired rigid body within a general serial or hybrid flexure system. We introduce a $6B\times1$ load vector, $\mathbf{\Gamma}$, that consist of 6×1 wrench vectors, $\mathbf{W_k}$, that each model an individual actuation load imparted on a corresponding rigid body labeled k within a general serial or hybrid flexure system as

$$\mathbf{\Gamma} = \begin{bmatrix} \mathbf{W}_1^T & \mathbf{W}_2^T & \dots & \mathbf{W}_B^T \end{bmatrix}^T \quad , \tag{2.1}$$

where B is the total number of rigid bodies within the system (excluding fixed or grounded bodies). For the system of Figure 3A (shown again in Figure 6), B is 2. The infinitesimal displacements of each of the system's bodies as a result of these loads is given by the $6B\times1$ displacement vector, $\boldsymbol{\lambda}$, as

$$\boldsymbol{\lambda} = \begin{bmatrix} \mathbf{T}_1^T & \mathbf{T}_2^T & \dots & \mathbf{T}_B^T \end{bmatrix}^T \quad , \tag{2.2}$$

where $\mathbf{T_j}$ is the 6×1 displacement twist vector that corresponds with body *j*. Note that twist vectors are traditionally defined as velocity vectors, but for this section we define $\mathbf{T_j}$ as the traditional twist vector multiplied by an infinitesimal unit of time (i.e., a displacement twist vector).

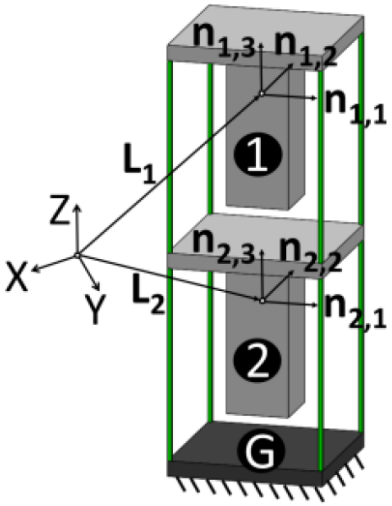

Figure 6: Parameters for constructing matrix [*M*]

The equation that relates the load and displacement vectors from Equation (2.1) and (2.2) is given by

$$\mathbf{\Gamma} = [M]\ddot{\boldsymbol{\lambda}} + [K]\boldsymbol{\lambda} \quad , \tag{2.3}$$

where [*M*] is the system's 6*B*×6*B* mass matrix and [*K*] is the system's 6*B*×6*B* stiffness matrix. Note that Equation (2.3) does not consider the effects of damping. The mass matrix, [*M*], is

$$[M] = diag\left([M_1] \;\; [M_2] \;\; ... \;\; [M_B]\right) \quad , \tag{2.4}$$

where *diag* is a function that creates a matrix filled with zeroes except for its diagonal components, $[M_e]$. These 6×6 matrices each pertain to body *e* and are defined by

$$[M_e] = [N_e][\Delta][In][N_e]^{-1} \quad , \tag{2.5}$$

where $[N_e]$ is a 6×6 matrix defined by

$$[N_e] = \begin{bmatrix} \mathbf{n}_{e,1} & \mathbf{n}_{e,2} & \mathbf{n}_{e,3} & \mathbf{0} & \mathbf{0} & \mathbf{0} \\ \mathbf{L}_e \times \mathbf{n}_{e,1} & \mathbf{L}_e \times \mathbf{n}_{e,2} & \mathbf{L}_e \times \mathbf{n}_{e,3} & \mathbf{n}_{e,1} & \mathbf{n}_{e,2} & \mathbf{n}_{e,3} \end{bmatrix} \quad , \tag{2.6}$$

and where $\mathbf{n}_{e,1}$, $\mathbf{n}_{e,2}$, and $\mathbf{n}_{e,3}$ are orthogonal 3×1 dimensionless unit vectors that correspond with body *e*, $\mathbf{0}$ is a 3×1 vector of zeroes, and $\mathbf{L}_e$ is a 3×1 location vector that points from the coordinate system's origin to the center of mass of body *e* (Figure 6). Note that the coordinate system of Figure 6 is different from that of Figure 3A. This was done to clarify the other parameters labeled in Figure 6 and to demonstrate the principle that the choice of coordinate system does not matter to the calculations of this section. The 6×6 matrix, [Δ], in Equation (2.5) is defined by

$$[\Delta] = \begin{bmatrix} [0_{3x3}] & [I_{3x3}] \\ [I_{3x3}] & [0_{3x3}] \end{bmatrix} \quad , \tag{2.7}$$

where $[0_{3\times3}]$ is a 3×3 matrix of zeroes and $[I_{3\times3}]$ is a 3×3 identity matrix. The 6×6 matrix, $[In_e]$, in Equation (2.5) is defined by

$$\left[In_e\right] = diag\left[\begin{array}{cccccc} I_{e,1} & I_{e,2} & I_{e,3} & m_e & m_e & m_e \end{array}\right] \quad , \tag{2.8}$$

where $I_{e,1}$, $I_{e,2}$, and $I_{e,3}$ are the mass moments of inertia of body e about axes that intersect the location $\mathbf{L_e}$ (Figure 6) and point in the directions of $\mathbf{n}_{e,1}$, $\mathbf{n}_{e,2}$, and $\mathbf{n}_{e,3}$, respectively. Thus the directions of $\mathbf{n}_{e,1}$, $\mathbf{n}_{e,2}$, and $\mathbf{n}_{e,3}$ do not matter as long as they correspond with $I_{e,1}$, $I_{e,2}$, and $I_{e,3}$. The scalar value m_e is the mass of body e.

The stiffness matrix $[K]$ in Equation (2.3) can be constructed for a general serial or hybrid system using the theory provided in [45]. The construction of this matrix depends only on the location, orientation, geometry, and material properties of the flexure elements within the system. If we now apply sinusoidal loads to a system's bodies such that they possess the same driving frequency, ω, Equation (2.3) can be rewritten as

$$\mathbf{\Gamma} = \left(-\omega^2\left[M\right] + \left[K\right]\right)\boldsymbol{\lambda} \quad . \tag{2.9}$$

If we define a new $6B\times6B$ matrix $[\Pi]$ according to

$$\left[\Pi\right] = \left(-\omega^2\left[M\right] + \left[K\right]\right)^{-1} \quad , \tag{2.10}$$

we can calculate the actuation load, $\mathbf{W_{k,i}}$, acting on a body labeled *k* within a serial or hybrid system that is necessary to drive another body labeled *j* in the same system with a displacement twist of $\mathbf{T_{j,i}}$ at a frequency of ω according to

$$\mathbf{W_{k,j}} = \left[\Pi\left(6j-5:6,6k-5:6k\right)\right]^{-1}\mathbf{T_{j,i}} \quad . \tag{2.11}$$

In Equation (2.11) we introduce a convention for creating a sub-matrix from within a larger matrix. If, for instance, we wish to create a sub-matrix that contained the components of rows *a* through *b* and of columns *c* through *d* from a matrix [*A*], we would write [*A*(*a*:*b*,*c*:*d*)] using the convention from Equation (2.11). Thus the static actuation space acting on any rigid body labeled *k* within a general serial or hybrid flexure system can be determined by linearly combining all the wrench vectors, $\mathbf{W_{k,i}}$, that result when all the independent twist vectors, $\mathbf{T_{j,i}}$, within the freedom space of the system's stage labeled *j* (i.e., the system's DOFs) are applied to Equation (2.11) with a speed, ω, of zero. Recall that the subscript *i* refers to the number of the DOF labeled. The dynamic actuation space acting on the same body *k* may be determined by linearly combining similar wrench vectors generated using Equation (2.11) for the same DOF twist vectors, but at all speeds (i.e., ω equals all real values). In practice, only a few different values of ω need to be applied to Equation (2.11) before the dynamic actuation space can be generated.

2.3 Micro-actuators Actuation Physics

2.3.1 Actuation Types

In this dissertation, we investigate in the types of actuator that can potentially be embedded in a microarchitectured unit to drive the displacement or deformation of the microstructures. The

discussion includes five primary types of actuators that will be referred to as *(1)* plate, *(2)* comb, *(3)* thermal, *(4)* Lorentz, and *(5)* piezo actuators in this paper. Other reviews of potential MEMS actuators can be found in a variety of publications [46–48].

(1) Plate actuators generate an attractive electrostatic force between two electrically conductive parallel plates when a voltage is applied. It is one of the most utilized actuators in micro-device designs in part because they *(i)* are compact, *(ii)* respond quickly to input voltage signals, *(iii)* generate minimal heat, *(iv)* require little power, *(v)* exhibit a direct mapping between voltage values and corresponding actuation forces, and *(vi)* are easily fabricated. Additionally, these actuators are well suited for actuating MEMS devices since their force density (i.e., the amount of force that can be generated per volume of the actuator) scales favorably as the device becomes smaller. Since such actuators only consist of two simple plates, they can often be fabricated on scales near the size of the smallest achievable feature size of the microfabrication process used to make them. Plate actuators are also force-based non-contact actuators that can generate forces on mirror elements without directly contacting or touching them. Thus, such actuators are well suited for actuating multi-DOF microstructures since each actuator will not shear off or impart harmful forces on other actuators while they drive their corresponding motion DOF because none of the actuators are mechanically joined to the mirror element that they actuate.

There are, however, drawbacks to using plate actuators. The ranges of motion of microstructures using electrostatic plate actuation are typically limited because the gap distances between the actuator plates must be small enough to achieve sufficient forces to actuate the system, but small gap distances geometrically restrict the amount the actuator plates can displace toward each other. Moreover, the electrostatic forces generated by plate actuators change nonlinearly as

the gap distance between their plates changes. This nonlinear force-displacement relationship makes the control of plate-actuated designs difficult especially if they possess multiple DOFs [49]. It also makes plate actuators susceptible to shorting failures due to pull-in instabilities that arise from the high sensitivity of plate position [50,51]. Furthermore, effects such as electric-field fringes along the edges of the moving flat plates and squeeze film damping that occurs between the plates can be difficult to model for achieving accurate control. Finally, plate actuators are unipolar actuators that can only pull the plates together in one direction (i.e., they cannot push the plates apart in the other direction).

(2) Comb actuators achieve many of the same advantages of plate actuators because they operate using similar electrostatic principles, but they differ from plate actuators in that they consist of a pair of comb-shaped geometries with interdigitated teeth instead of flat parallel plates. Comb-actuated designs are significantly easier to control than plate-actuated designs because the electrostatic attractive forces that they generate are independent of the separation distance between their comb bodies. Thus, such designs can typically achieve significantly larger ranges of motion than plate-actuated designs while maintaining a constant and sufficiently large actuation force to drive the system's mirror elements over their full stroke with high speeds.

Although they are also force-based, non-contact actuators similar to plate actuators, the interdigitated geometry of comb actuators restricts their relative motions more than the simple geometry of plate actuators, which leads to some challenges. One such challenge is that comb actuators typically require more complicated flexure bearings to carefully guide their intended motions so that the teeth of the combs do not collide and short at any point as they are moved along their full range of motion. If comb-actuated microstructure designs possesses multiple DOFs, it is

also important that additional flexures be implemented into the designs so that their actuators are decoupled [52] (i.e., when one set of combs is actuated within the system, the other sets of combs are not moved in unwanted directions that could cause them to short). Thus, due to the fact that comb-actuated designs typically require complex flexure designs and possess tightly packed comb-teeth geometries, the fabrication complexity and cost of most comb-actuator designs are often high compared to designs that utilize different actuator types [53]. Moreover, since the comb teeth of comb-actuated designs must be as large or larger than the smallest feature size that can be achieved by the available microfabrication process, the smallest achievable versions of comb-actuated designs are typically significantly larger than the smallest achievable versions of plate-actuated MMA designs fabricated using the same process. Finally, note that similar to plate actuators, comb actuators are also unipolar actuators.

(3) Thermal actuators used for microarchitecture actuation are typically structures that are layered with materials that possess large differences in their thermal expansion coefficients. These actuators are actuated by flowing current through their geometries, which heats their layers and causes the actuators to bend in one or two different directions (i.e., unimorph or bimorph electrothermal actuators respectively) due to the thermal mismatch between their constituent layers. Although thermally actuated materials typically exert large forces as they expand or contract small amounts, the unimorph and bimorph thermal actuators are designed to lessen these often unnecessarily large actuation forces to gain impressively large displacement capabilities via transmission principles. Since thermal actuators are relatively simple geometries, they are also typically easy to fabricate and can be made on scales that are comparable to the smallest feature size that can be achieved by the microfabrication process used to make them.

Thermal actuators also exhibit inherent drawbacks. Although, the temperature of structures can generally change more rapidly as their size decreases, thermal actuators typically achieve relatively slow speeds at micro-scale(i.e., less than 1kHz) compared with other MEMS actuators [54]. These actuators are also difficult to control and do not achieve high accuracy or precision due to the complex nature of heating and cooling (i.e., there is not a direct mapping between the current that flows through their geometry and the amount that they displace because of thermal dynamics). Furthermore, such actuators require high amounts of power compared to other MEMS actuators since much of the power given to the system is dissipated in the form of heat, which can cause damage or unwanted thermal expansion effects to other features within the microstructure. Finally, thermal actuators are displacement-based contact actuators that are directly joined to the bodies that they displace. Thus, complex flexures are typically required to decouple each of the thermal actuators within multi-DOF microstructure designs such that they don't jam, harm, or adversely affect one another during operation.

(4) Piezo actuators utilize piezoelectric materials that expand or contract upon application of a voltage. Since these materials typically exert large forces as they expand or contract small amounts, unimorph and bimorph designs that consist of layers of piezoelectric materials deposited on different material layers are used to achieve significantly larger displacement capabilities while reducing their output force capabilities as a tradeoff. Although piezo actuators exhibit many of the same advantages of thermal actuators since they operate using similar principles, they are distinguished from thermal actuators in that piezo actuators operate with relatively low power input and dissipate minimal amounts of heat.

Although piezo actuators can be fabricated at scales that approach the size of the smallest feature size achievable by available microfabrication processes due to their simple geometry, most existing microfabrication technologies are restricted to depositing only thin layers of piezo materials and the task of polarizing the piezo layers in the correct directions within multi-DOF microstructures is difficult. Additionally, since these actuators are displacement-based contact actuators, they also require complex decoupling flexures to drive designs with multiple DOFs.

(5) Lorentz actuators consist of trace coils attached to microstructure bodies, which are driven by Lorentz forces that result from current flowing through their geometry in the presence of carefully arranged magnetic fields that are produced by small magnets. As force-based non-contact actuators, Lorentz actuators achieve many of the same advantages of plate and comb actuators, but Lorentz actuators are also capable of bipolar actuation (i.e., they can push and pull in two directions). Moreover, Lorentz actuators can typically achieve larger forces than plate and comb actuators when the mirror is multiple millimeters or larger in size. Lorentz actuators can also achieve linear actuation (i.e., the current or voltage used to drive them is linearly proportional to the force that they generate), which simplifies and improves their control such that they achieve high speeds with excellent accuracy and precision even for multi-DOF scenarios.

Lorentz actuators are, however, complex and difficult to fabricate—particularly at small scales. The minimum widths of the traces that constitute the coils are limited by both the smallest feature size achievable by the available microfabrication process and the excessively high rate of heat dissipation that can be reached as the traces become too thin. Additionally, the total lengths of the traces that constitute the coils, which are proportional to the Lorentz forces generated, are limited by the area of the microstructures on which they are typically attached to. The strong

magnetic fields required by Lorentz actuators can cause damage to electronics or generate unwanted forces on neighboring micromirrors within the array via crosstalk, which can be difficult to manage.

2.3.2 Performance Comparison of Actuation Physics

To quantitatively compare the performance of different micro-actuation types, we reviewed the performance of all existing micromirror array (MMA) devices that have at least two rotational DOFs. MMA devices may be considered as a type of metasurfaces given the similarities in their design and function. MMAs consist of a periodic pattern of closely packed small mirrors (i.e., millimeter-sized or smaller) supported by microstructures, which can be actuated to steer or manipulate the phase of light. The microstructures that constitute such arrays can be controlled to achieve various combinations of tip, tilt, and/or piston degrees of freedom (DOFs) to manipulate the light that reflects off the array's mirror surface. Hundreds of different MMA designs have been proposed by research groups and commercial companies, which provides enough data to establish a valuable reference for comparing the performance of different actuation physics of active microarchitectured materials.

Figure 7A provides a performance plot that compares the actuator angular energy density of the MMA designs with their rotational full range of motion. Figure 7B provides a performance plot that compares the actuator angular energy density of the same designs with their pitch. Appendix A provides detailed definitions of these performance metrics. These plots also provide the actuator angular energy density limits for each type of actuator as shown by the colored dashed lines. These lines depict the derived bounds that theoretically should not be exceeded by current

or future MMA designs. The derivation details of each of these limits are provided in corresponding subsections of Appendix B.

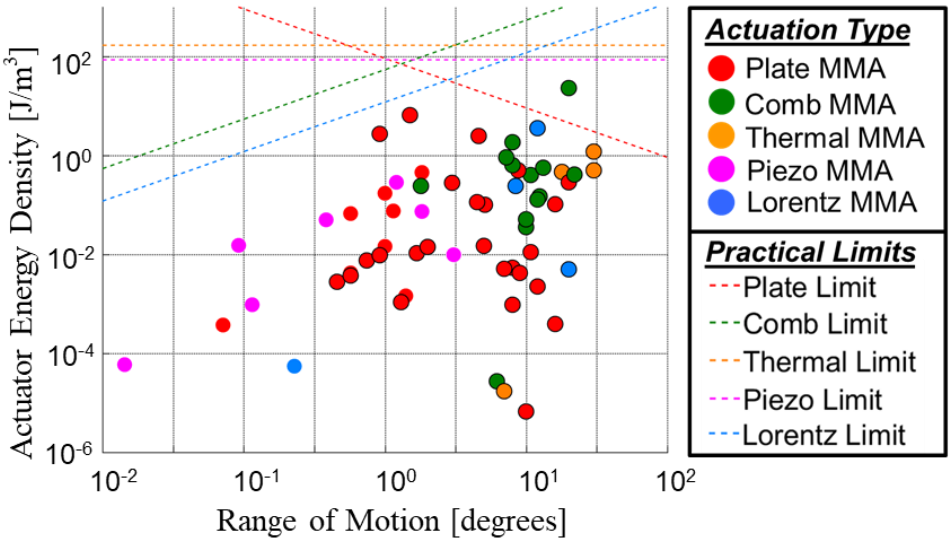

(A)

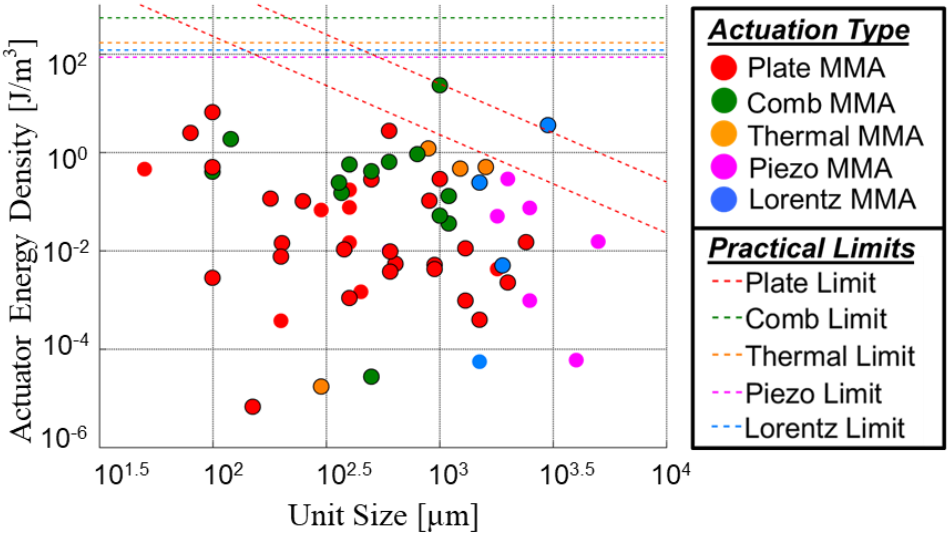

(B)

Figure 7: Analog-actuation 2D TT and TTP MMAs with actuator limits: angular energy density vs. rotational range (A); angular energy density vs. pitch (B).

Note from Figure 7A and B that the limits for thermal and piezo actuators are both a constant value, which are not dependent on any performance metrics. The limit for thermal actuators is higher than the limit for piezo actuators. Note also from Figure 7A and B that the limits for comb and Lorentz actuators are always parallel but are dependent on the rotational full range of motion. Both of these limits are plotted in Figure 7B using a rotational full range of motion of 10^{o}, which is a typical range of interest for most MMA applications. Note also that the limit for comb actuators is higher than the limit for Lorentz actuators. Finally, note from Figure 7A and B that the limit for plate actuators is dependent on the rotational full range of motion and on the array's pitch. This limit is plotted in Figure 7A using a pitch of 500μm and is plotted in Figure 7B using a rotational full range of motion of 10^{o}. Both of these values are typical for most MMA applications. Although it appears that design number 2 is closely approaching the plate limit shown in Figure 7B with a rotational full range of motion of 10^{o}, the more applicable limit for that particular design is shown as another dashed red line plotted using that design's rotational full range of motion, which is 0.92^{o}.

Chapter 3:

Optimization of Active Microarchitecture Design

Once the flexure design topology of an active microarchitectured material is synthesized, there is a need for a complementary follow-on tool that can optimize the geometric parameters of the topology solutions so final designs can be produced that best achieve desired performance requirements in addition to achieving the desired DOFs for given constituent materials. In this chapter, we introduce a computational tool that identifies the boundaries of the performance capabilities achieved by general flexure system topologies if their geometric parameters are allowed to vary from their smallest allowable feature sizes to their largest geometrically compatible feature sizes for given constituent materials. The boundaries fully define the design spaces of flexure systems and allow designers to visually identify which geometric versions of their synthesized topologies best achieve desired combinations of performance capabilities.

3.1 Introduction

To set up the optimization problem, a model needs to be established that describes the performance of an active architecture design with a given set of design parameters. This model can be *1)* a real experiment, of which the parameters can be arbitrarily changed and controlled, *2)* a numerical model based on finite element analysis, *3)* a closed-form analytical model of the parameterized topologies, or *4)* a regression model based on data generated by finite element analysis or real experiments. Note also that although the tool is introduced in this paper as a tool for optimizing

the parameters of flexure system topologies, it could also be applied to a host of other diverse applications.

Although few researchers have directly attempted system-performance boundary identification, its goal is similar to the goal of multi-objective optimization, which has been studied extensively. A multi-objective optimization problem (MOOP) deals with more than one objective function and aims at finding a set of solutions that optimizes all the objective functions simultaneously. Several methods have been proposed to solve the local or global Pareto-optimal solution set [55]. One of the most widely-used methods is the weighting method [55]. Haimes et al. [56] introduced the ε-Constraint method in 1971 and Yu [57] introduced the method of global criterion in 1973. Wierzbicki [58,59] introduced the achievement scalarizing function approach in 1981. Other solving methods include normal boundary intersection [60], evolutionary algorithm [61], lexicographic ordering [62], and goal programming [63]. More recently, MOOP methods have focused on stochastic algorithms, including a variety of evolutionary algorithms [64,65]. Such algorithms generate more reliable global Pareto-optimal solution sets, but require significantly more function evaluations than deterministic algorithms and are thus generally better suited for complex black-box-model optimizations. The boundary identification approach proposed in this paper has in part been adapted from various deterministic multi-objective optimization methods such that the complete continuous boundary (including concave portions) that circumscribe the performance capabilities achieved by general flexure topologies can be identified and refined with a desired accuracy.

By combining the utility of this computational tool with the current FACT approach, a new advantageous approach emerges, which is unique from other existing design-optimization

approaches. Whereas other approaches (e.g., topology optimization [66–68] or module optimization [69]) simultaneously combine the tasks of optimizing a design's topology with its geometry, the proposed approach decouples those tasks in such a way that the time-consuming computations are reserved solely for the simpler task of geometry optimization only. This optimization occurs after the FACT approach has directly generated and finalized the most promising topologies without performing expensive iterative calculations. Thus, by decoupling the tasks of topology synthesis and geometry optimization in this way, the speed that optimal designs can be generated from start to finish as well as the likelihood that the global-optimum solutions are identified increases.

3.2 Performance Boundary Identification

The optimization problem is set up that the design parameters of a flexure-system topology are the model's inputs, x_i, and the performance capabilities achieved by the design instantiations that are defined by these corresponding input parameters are the model's outputs, f_j. Constraint functions are also provided to define what combination of input values are permissible.

The boundary-searching algorithm consists of two main processes, *directional maximization* and *gap reduction*. Both processes rely on an optimization approach that implements two numerical optimization methods, the Sequential Quadratic Programming (SQP) [70,71] algorithm and Augmented Lagrangian Pattern Search (ALPS) [72–74] algorithm, to achieve the local extremum of an objective function.

In each local optimization process, the SQP method is implemented first. The SQP method starts with a given initial guess, and attempts to compute, or "step to", another point that is "closer"

to the local extremum. At each point, the gradient (derivatives) and Hessian matrix (the symmetric matrix of second derivatives) of the objective function are approximated using adjacent points, and then used to construct a Quadratic Programming (QP) sub-problem [75]. The solution of this QP sub-problem is used to compute the step towards the next point. The SQP process terminates when the "step" is smaller than a prescribed resolution of the input parameter in all directions x_i, or when it fails to generate the next point, which typically occurs because the derivatives or second derivatives of the specific objective function cannot be correctly evaluated to set up the QP sub-problem.

After the SQP process terminates, the algorithm continues the optimization process by implementing the ALPS method to solve for the local extremum of the same objective function starting at the point corresponding to the best inputs (that generate the largest or smallest objective function value) identified using the SQP method. The ALPS algorithm searches for a better value of the augmented Lagrangian function [33] among a set of points, called a *mesh*, located around the current point (mesh center point) at a distance, $\pm r_i$, along the direction of each input parameter x_i. The distance r_i is called the *mesh size* and is initially chosen to be a value between 10% to 30% of the total range of each x_i. If among the mesh points there is a point that improves the value of the augmented Lagrangian function over the current mesh center point, this point becomes the new center point in the next step and the mesh size r_i increases by a factor of k, which is typically set to be 2. If, on the other hand, no improvements can be achieved from all the mesh points around the center point, the meshing size decreases by a factor of k. By taking these iterative steps, the objective function converges to its extremum value. The ALPS process terminates when the mesh size is smaller than the prescribed resolution in every direction.

A theoretical example of a system with only two inputs, x_1 and x_2, will be used to conceptually explain how the boundary searching algorithm utilizes the local optimization approach to plot a concave boundary that circumscribes the system's full design space for two of the system's achievable outputs, $f_1(x_1, x_2)$ and $f_2(x_1, x_2)$. For the theoretical example of this section, the constraint function is shown as the red spline boundary line in Figure 8A.

The algorithm begins with the directional maximization process. Starting at an initial guess, this algorithm first identifies a set of other permissible input combinations that result from adding and subtracting the resolution increment of each input, Δx_i, to and from the first randomly selected combination of inputs along each input's axis. For the example of Figure 8A, this first set of input combinations are shown as the four blue dots immediately surrounding the blue dot labeled $O_{1,1}$. Note that although Δx_1 is shown as being equal to Δx_2 in the example, these resolution increments do not have to be equal for other scenarios. The system's model is then used to map all of the combinations of these inputs to their corresponding combinations of outputs, which are represented by the five blue dots shown in Figure 8B. Note that the original input dot, $O_{1,1}$, maps to the output dot, $Z_{1,1}$. The SQP algorithm then approximates the gradient and Hessian matrix of the objective function defined by

$$J\left(x_1, x_2\right) = \cos\left(\theta\right) f_2\left(x_1, x_2\right) + \sin\left(\theta\right) f_1\left(x_1, x_2\right), \tag{3.1}$$

using the input and output combinations (i.e., the adjacent blue dots in Figure 8A and Figure 8B), where θ is initially set to 0 so that the largest f_2 output can be pursued first. This gradient and

Hessian matrix are then used to construct a QP sub-problem. In the example of Figure 8, suppose the new combination of inputs determined is shown as the red dot labeled $O_{1,2}$ in Figure 8A. Note that this dot's corresponding combination of outputs, which is shown as the red dot labeled $Z_{1,2}$ in Figure 8B, possesses an f_2 value that is larger than any of the other previous blue dots shown in the same figure. The SQP algorithm then repeats this process by finding a new set of permissible input combinations. For the example of Figure 8A this new set of input combinations are shown as the four red dots immediately surrounding the red dot labeled $O_{1,2}$. Note that each of the five red dots in Figure 8A map to a corresponding red dot in Figure 8B. In this manner, the SQP algorithm rapidly finds an efficient path toward a local maximum of the objective function by iteratively stepping from one cluster of dots to the next.

After the SQP algorithm terminates, the boundary-plotting algorithm continues the optimization process by supplying the combination of permissible inputs that map to the combination of outputs that produce the largest objective-function value identified by the SQP algorithm to the Augmented Lagrangian Pattern Search (ALPS) optimization algorithm. For the example of Figure 8A, suppose the SQP process was unable to step beyond the cluster of dots surrounding $O_{1,2}$ and thus terminated at that location. The combination of inputs that would be supplied to the ALPS algorithm would be the red dot labeled $O_{1,3}$ in Figure 8A since this combination of inputs maps to the combination of outputs that achieve the largest f_2 value found using the SQP algorithm. This combination of outputs is shown as the red dot labeled $Z_{1,3}$ in Figure 8B. The ALPS algorithm first identifies a set of other permissible input combinations that result from adding and subtracting an initial mesh size, r_i, to and from the combination of inputs supplied to the algorithm along each input's axis. The initial mesh size, labeled r_2 in Figure 8A, is set to

20% of the range of its corresponding input parameter (i.e., $r_i=0.2|x_{i,max}-x_{i,min}|$). For the example of Figure 8A, the first set of ALPS-generated input combinations are shown as the four purple dots surrounding the red dot labeled, $O_{1,3}$. Note that although r_1 is shown as being equal to r_2 in the example, these mesh sizes are not typically equal for other scenarios. The system's model is then used to map the combinations of these inputs to their corresponding combinations of outputs, which are represented by the four purple dots shown in Figure 8B. The ALPS algorithm then identifies if any of these combinations of inputs map to a combination of outputs that produce an objective-function value that is larger than any produced previously in the optimization process. Suppose, for instance, that the input combination of the example in Figure 8A, labeled $O_{1,4}$, maps to the output combination, labeled $Z_{1,4}$ in Figure 8B, which achieves the largest f_2 value previously identified. The ALPS algorithm would then step to the dot representing that input combination (e.g., $O_{1,4}$). The algorithm would then identify a set of other permissible input combinations that result from adding and subtracting the previous mesh size (e.g., r_i in this case) multiplied by an expansion factor to and from this combination of inputs along each input's axis. The expansion factor is set to 2. Thus, for the example of Figure 8A, the next set of ALPS-generated input combinations are shown as the three orange dots surrounding the purple dot labeled, $O_{1,4}$. These orange input dots shown in Figure 8A map to the three orange output dots shown in Figure 8B. The algorithm then identifies if any of these output combinations produce an objective-function value that is larger than any produced previously in the optimization process. Since none of the orange dots in Figure 8B possess an f_2 value that is larger than $Z_{1,4}$, the ALPS algorithm would then identify a set of other permissible input combinations that result from adding and subtracting the previous mesh size (e.g., $2r_i$ in this case) divided by the same expansion factor to and from the

combination of inputs labeled $O_{1,4}$ in Figure 8A along each input's axis. Thus, for the example of Figure 8A, the next set of ALPS-generated input combinations are shown as the three light-green dots surrounding the same purple dot labeled $O_{1,4}$. These light-green input dots shown in Figure 8A map to the three light-green output dots shown in Figure 8B. Again, since none of the light-green dots in Figure 8B possess an f_2 value that is larger than $Z_{1,4}$, the ALPS algorithm would then identify another set of other permissible input combinations that result from adding and subtracting the previous mesh size (e.g., r_i in this case) divided by the same expansion factor to and from the combination of inputs labeled $O_{1,4}$ in Figure 8A along each input's axis. Thus, for the example of Figure 8A, the next set of ALPS-generated input combinations are shown as the four dark-green dots surrounding the same purple dot labeled $O_{1,4}$. This process repeats until either *(i)* one of the new input combinations maps to an output combination with an objective-function value that is larger than any produced previously, or *(ii)* the mesh size becomes equal to or less than a specified input tolerance, which for this paper is set to the resolution of the input parameters, Δx_i. If the first option *(i)* occurs, the algorithm will step to the improved input combination and the ALPS process will continue iterating. If the second option *(ii)* occurs, the ALPS algorithm will terminate. For the example of Figure 8A, the second option occurred because the mesh size of the four yellow dots shown immediately surrounding the purple dot, labeled $O_{1,4}$, is equal to Δx_2, labeled in the same figure, and none of the new output dots generated ever surpassed the f_2 value of $Z_{1,4}$ as shown in Figure 8B.

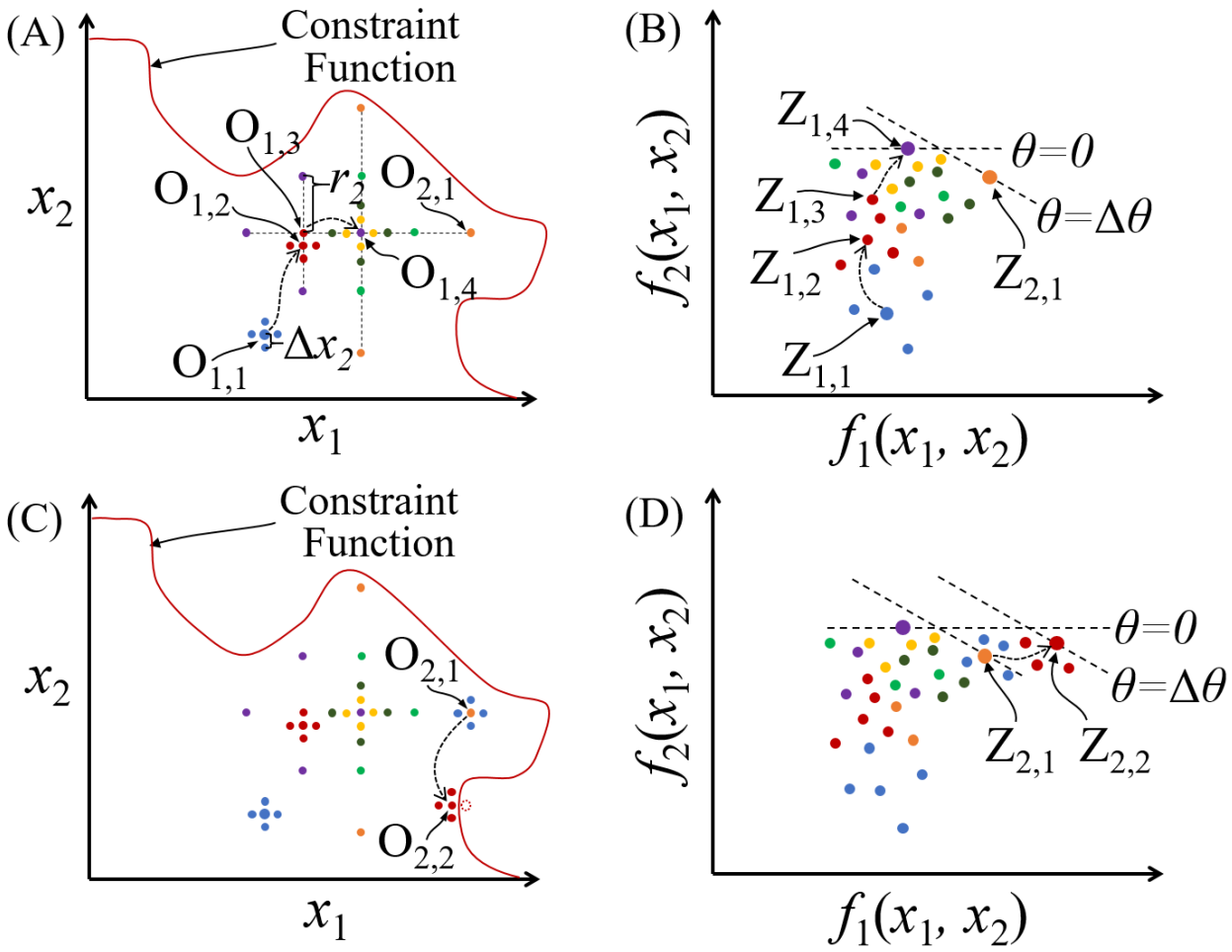

Figure 8: Progression of the SQP and then ALPS optimization algorithms for θ=0 initialized in the objective function in the input space (A) and in the corresponding output space (B); continued progression of the same optimization algorithms for $\theta=\Delta\theta$ incremented in the objective function in the same input space (C) and in the same output space (D)

Once the SQP and then ALPS algorithms have both run their full course for determining the maximum value of $J(x_1, x_2)$ from Equation (3.1) for θ=0, the θ parameter is then incrementally increased by $\Delta\theta$, which is typically set to a value between $\pi/10$ to $\pi/20$. Using this new θ parameter, the algorithm then computes the value of the objective function in Equation (3.1) for all existing

input combinations, which for the example of this section are shown as the dots in Figure 8A. From among these input combinations, the one that produces the largest objective function value for $\theta=\Delta\theta$ corresponds to the input combination represented by the dot labeled $O_{2,1}$ in Figure 8A, which maps to the output combination represented by the orange dot labeled $Z_{2,1}$ in Figure 8B. The algorithm would then supply this input combination to the SQP algorithm to generate more input combinations that produce larger objective function values as described previously. The four blue dots immediately surrounding the dot labeled $O_{2,1}$ in Figure 8C would be identified first for the example of this section using this approach. Those four blue dots map to the four new blue dots shown in Figure 8D that surround the dot labeled $Z_{2,1}$. The SQP algorithm would then identify the next input combination (e.g., $O_{2,2}$ shown in Figure 8C) that produces a larger objective function value. Note that the input combination dot, $O_{2,2}$, maps to an output combination dot, labeled $Z_{2,2}$ in Figure 8D, that is farther away along the direction prescribed by the new θ parameter value (i.e., $\Delta\theta$). As the SQP algorithm continues, four other input combinations would be identified that immediately surround the input combination dot labeled $O_{2,2}$ in Figure 8C. These dots are colored red in Figure 8C. The SQP algorithm would continue in this way until it terminates. The ALPS algorithm would then take over where the SQP algorithm left off as described previously until the ALPS algorithm also terminates. Once the ALPS algorithm terminates, the algorithm will have found the input combination that achieves the largest objective function value identified from among those previously tested for $\theta=\Delta\theta$.

The algorithm iterates this pattern of steps to identify the combinations of output values that lie farthest away along their prescribed directions defined by their corresponding θ value in a clockwise fashion until $\theta\geq 2\pi$ (i.e., all the directions have been swept). It is important to note that

any time before the θ parameter is incrementally advanced, the objective function of Equation (3.1) is rechecked for every combination of input values that have been evaluated up to that point to make sure that each of the previously identified output dots that used to be the farthest away along their prescribed directions are still the farthest away. If a new dot is ever identified that is farther away than a previous dot along a specific direction, θ, (i.e., if a new dot exceeds the dashed lines in Figure 8B), the iterative process is reset to that direction and the process continues using that improved output dot.

Once the directional maximization process is complete, the alpha shape of all the combinations of the output value points are identified and plotted as the boundary. Many systems produce a cloud of output dots that form a concave—not convex—region like the one shown in Figure 9A. If the boundary of such a cloud of output dots are identified, the result would be the red boundary shown in Figure 9B. This boundary would grossly overestimate the actual system's achievable performance space since it is convex instead of concave like the cloud of output dots. Thus, to address this issue, the algorithm adopts the gap reduction process to reduce the size of the gap along the boundary curve.

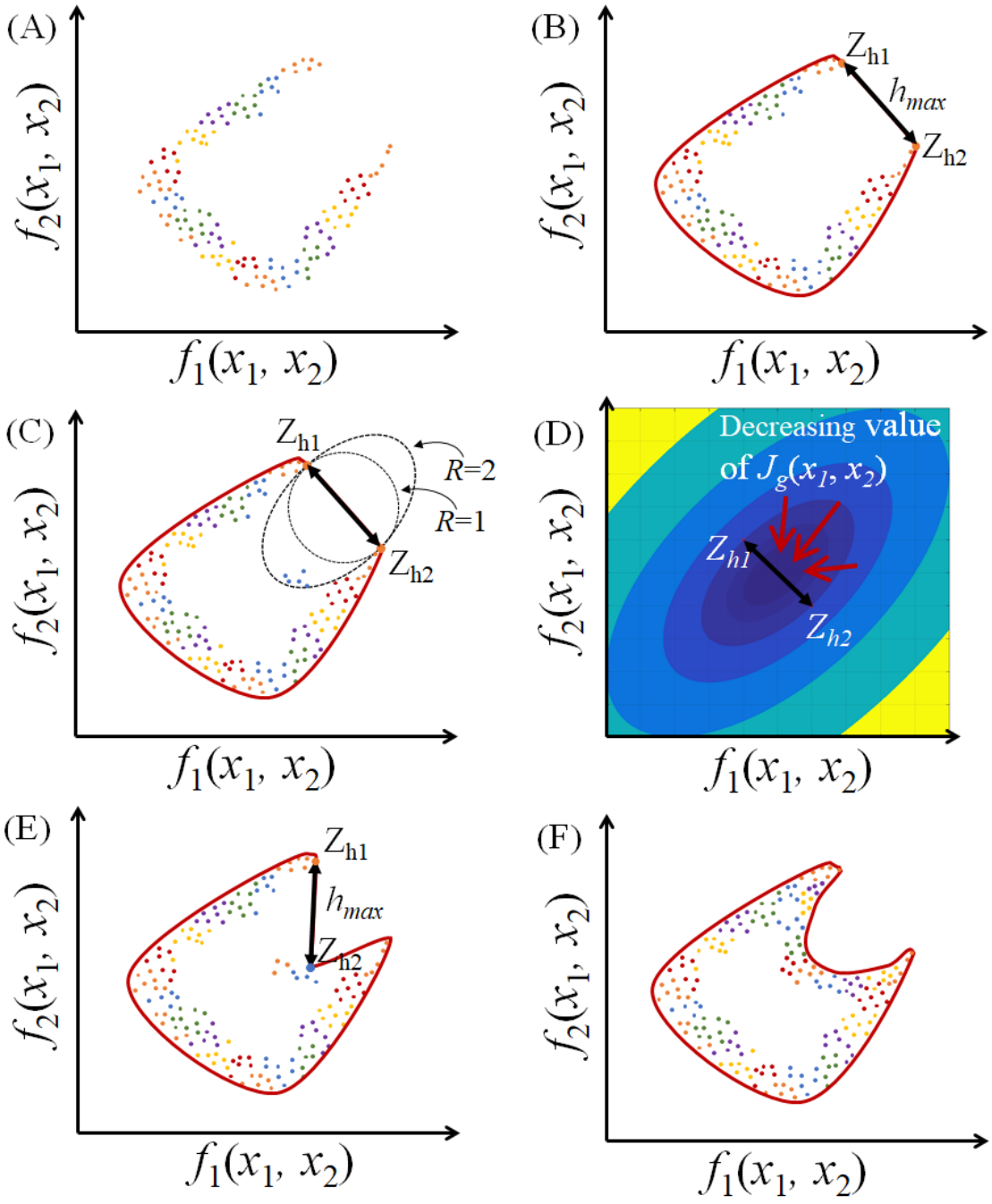

Figure 9: Generated output dots (A); convex boundary first identified (B); new objective function minimized to identify other output dots within circular or elliptical regions (C); elliptical contour diagram of the new objective function with R=2 (D); boundary updated with a new h_{max} value (E); process successfully identifies boundaries that are concave (F)

This gap reduction process starts with identifying all the vectors that point from each output dot along the existing boundary to their neighboring dots on the same boundary. The magnitude, h_{max}, of the longest vector is identified because this vector points between the two output dots (e.g., Z_{h1} and Z_{h2} shown in Figure 9B) that usually correspond to the opening of a previously unknown concave boundary. The algorithm then computes a new objective function, $J_g(x_1, x_2)$, defined by

$$\begin{aligned} J_g(x_1,x_2) = & \left(\frac{\cos^2\alpha}{R^2}+\sin^2\alpha\right)\left(f_1(x_1,x_2)-\frac{f_{1,Zh1}+f_{1,Zh2}}{2}\right)^2 \\ & +\left(\frac{\sin^2\alpha}{R^2}+\cos^2\alpha\right)\left(f_2(x_1,x_2)-\frac{f_{2,Zh1}+f_{2,Zh2}}{2}\right)^2 \\ & +2\sin\alpha\cos\alpha\left(\frac{1}{R^2}-1\right)\left(f_1(x_1,x_2)-\frac{f_{1,Zh1}+f_{1,Zh2}}{2}\right)\left(f_2(x_1,x_2)-\frac{f_{2,Zh1}+f_{2,Zh2}}{2}\right) \end{aligned} \tag{3.2}$$

for all the input combinations that have been previously evaluated with R=1. This objective function is minimized to identify output combinations that lie within circular or elliptical regions like those shown in Figure 9C. If the R variable in Equation (3.2) is 1, the region is a circle. If, however, this variable increases, it becomes an increasingly elongated ellipse as shown in Figure 9C. The angle, α, in Equation (3.2) is defined by

$$\alpha = \arctan\left(\frac{f_{1,Zh2}-f_{1,Zh1}}{f_{2,Zh1}-f_{2,Zh2}}\right), \tag{3.3}$$

where $f_{1,Zh1}$ and $f_{2,Zh1}$ from Equation (3.2) and (3.3) are the horizontal and vertical components of the Z_{h1} dot labeled in Figure 9C, and $f_{1,Zh2}$ and $f_{2,Zh2}$ are the horizontal and vertical components of the Z_{h2} dot labeled in the same figure. After the computations of the objective function of Equation (3.2) for all the input combinations that have been previously evaluated for R=1, it identifies the existing input combination that produces the smallest objective function value. This input combination is the combination that maps to the output combination that is closest to the center of the circle shown in Figure 9C. If no output dots are found within the circle, the input combination corresponding to either the output dot Z_{h1} or Z_{h2} will be chosen as the closest to the center of the circle and is thus supplied to the SQP and then ALPS algorithm described previously to evaluate new input combinations. Suppose, for the example of Figure 9, that when this optimization is performed that the new group of blue output dots shown in Figure 9C is generated. Since none of these output dots lie within the center of the circle shown in the figure, the previous R value in the objective function of Equation (3.2) is multiplied by a factor of 2 and the search region is expanded to an ellipse shown in Figure 9C. Figure 9E shows the elliptical contour diagram of $J_g(x_1, x_2)$ for this R value (i.e. R=2). If no output dots are found within the new ellipse, the process continues to iterate by multiplying the previous R value by the same factor of 2 to increase the elliptical search region further. For the example of Figure 9C, however, there are output dots that lie within the elliptical search region corresponding to an R value of 2. Thus, the input combination that maps to the output dot that lies within this region and possesses the smallest objective function value for R=2 is supplied to the SQP-ALPS optimization algorithm to identify an even better output dot that achieves an even smaller objective function value. This process will produce new output dots (e.g., the new set of orange dots shown in Figure 9E). Whether these new output dots achieve a smaller

objective function value or not, the output dot that achieves the smallest objective function value is identified and considered part of the system's performance boundary. It is thus redefined as either Z_{h1} or Z_{h2}. In the example of Figure 9E, the Z_{h2} output dot is the one that is redefined. Note also that h_{max} is also updated. This boundary learning process is repeated until both *(i)* the horizontal component of the boundary vector with the largest magnitude (i.e., h_{max}) is less than a set percentage of the horizontal distance across the full cloud of output values, and *(ii)* the vertical component of the same vector is also less than the same percentage of the vertical distance across the same cloud. This percentage threshold is typically set between 5% and 10%. Additionally, before the largest boundary vector is updated with a new magnitude (i.e., h_{max}), the entire optimization process of this section is repeated using the previous objective function in Equation (3.2) for all θ values to ensure that any new dots evaluated since using that objective function are allowed to improve the boundary's accuracy if possible. In this way both convex and concave boundaries, like the concave boundary shown in Figure 9F, can be identified that accurately define the system's achievable performance space.

Chapter 4:

Active Microarchitectured Metamaterial Designs

In this chapter, we introduce two active microarchitectured metamaterial designs. We first introduce an active microarchitectured material that utilizes piezo actuators to achieve programmable mechanical properties. The performance of the design topology is generated for all possible geometric parameter combinations. The result is compared with the boundary identified using the computational tool introduced in Chapter 3. A second active microarchitectured material design is then introduced that is based on electrothermal actuators. The optimal geometric parameters are identified to generate the optimal performance, and the corresponding designs are fabricated.

4.1 A Piezo-actuated Microarchitectured Material

4.1.1 Design

The active microarchitectured material (Figure 10) introduced in this section consists of a large periodic lattice of small compliant unit cells (i.e., <5mm) that are independently controlled using piezo actuators, sensors, and microprocessors embedded within each cell. This material exhibits desired bulk mechanical properties according to control instructions that are uploaded to the material's microprocessors.

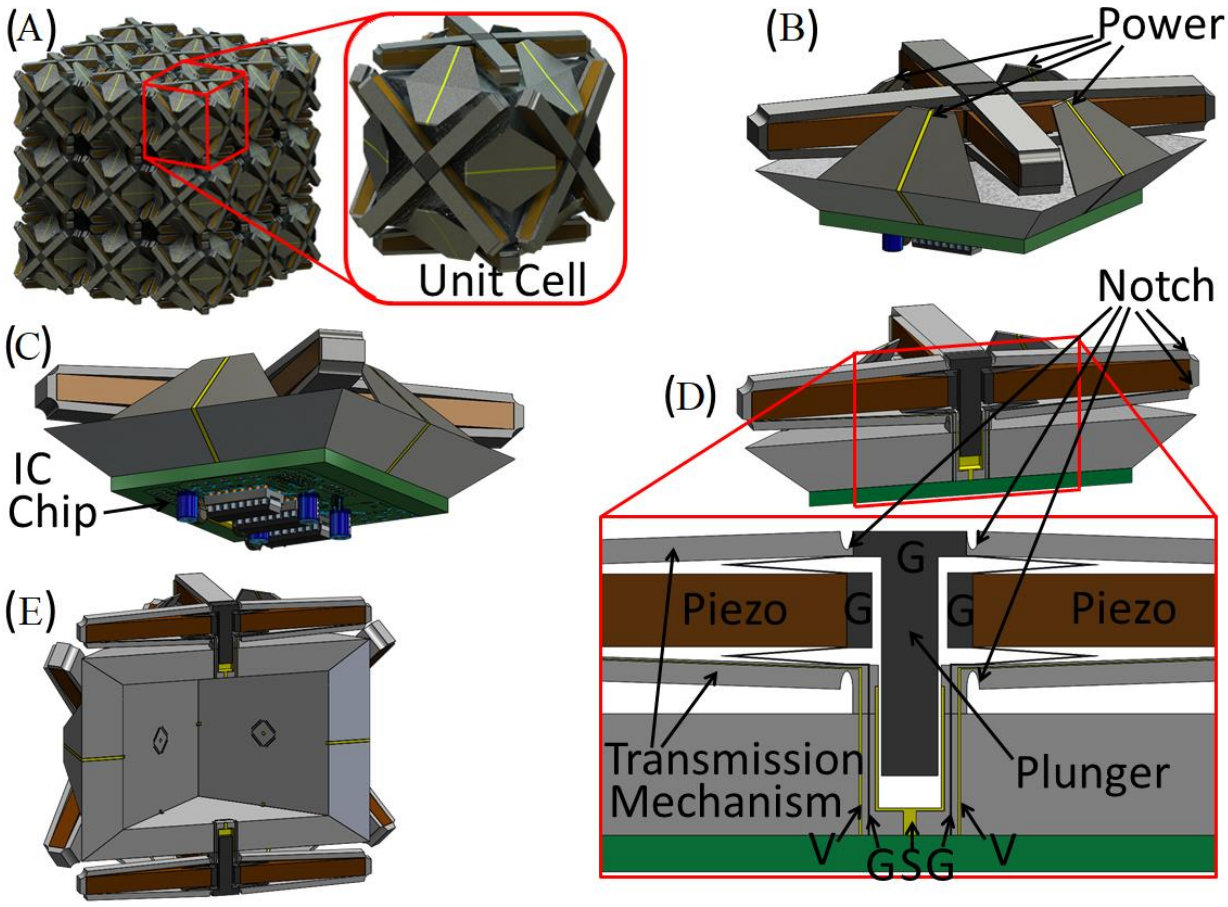

Figure 10: Active microarchitectured material lattice design (A), its cell's repeated sector (B and C), a cross-section of the sector (D), and a cross-section of the unit cell (E)

To understand how the proposed material achieves programmable properties, consider the periodic lattice of unit cells shown in Figure 10A. Each cube-shaped unit cell consists of the same sector design (Figure 10B and C) repeated six times within the cube. At the center of each unit cell is a microprocessor or integrated circuit (IC) chip, labeled in Figure 10C, that functions as the brain of each cell. Conductive lines, labeled 'Power' in Figure 10B, run down the middle of trapezoid-shaped blade flexures to power the IC chip from an external source. The trapezoid-shaped blade

flexures are designed to deform such that the unit cells are permitted to move with respect to one another as desired while simultaneously constraining the unwanted relative shear and torsional motions. Note that the lattice's unit cells join together along the top faces of these trapezoid-shaped blade flexures as well as along the top face of each sector's plunger, labeled in Figure 10D. The cross-sectional view of Figure 10D details how the cell's IC chip could also be electrically grounded by an external source. The darkest grey regions, labeled 'G' in Figure 10D, are conductive and are connected to an electrical ground. Note from the isometric view in the top portion of Figure 10D that the two bodies labeled 'G' on either side of the plunger in the bottom portion of the same figure are joined together as part of the same rigid body with a hole down its central axis through which the plunger is designed to translate. Each sector's four piezo actuators, labeled 'Piezo' in Figure 10D, span between this electrically grounded body at one end and a different conductive electrode at their other end. These electrodes are wired directly to the cell's IC chip via the lines labeled 'V' in Figure 10D. If the IC chip imparts a positive or negative voltage on these 'V' lines, the piezo actuators will expand or contract causing the plunger to move down or up respectively due to the fact that the actuators are placed within a compliant transmission mechanism, labeled in Figure 10D. This transmission mechanism causes the displacement of the plunger to amplify the displacement of the actuators while also causing the plunger's output force capability to attenuate the actuators' output force capability. This transmission effect is important because piezo actuators inherently exhibit abundant output force capabilities but do so over limited ranges of strain. Thus, by adjusting the geometry of the transmission mechanism, designers can tune the lattice such that it achieves a useful range of programmable properties over a large range of strains. Note also that the transmission mechanism utilizes notch flexures, labeled 'Notch' in

Figure 10D, which cause small localized regions of deformation that maximize the transmission efficiency of the mechanism by minimizing the amount of strain energy stored in the compliant structure. Notch flexures also enhance the design's functionality because they are less likely to cause failure due to buckling compared with other flexure element alternatives (e.g., blade or wire flexures). Note also that the axes of the design's piezo actuators are aligned along the diagonal directions of the cube-shaped unit cell's square faces. This alignment allows the piezo actuators to be as long as possible such that their range of expansion and contraction can be maximized. Although the four piezo actuators are used to drive the sector's plunger along its axis, a sleeve-like capacitive sensor that surrounds the plunger could be used to sense its position. As the electrically grounded plunger translates along its axis, the conductive region that surrounds the bottom-portion of the plunger, colored yellow in Figure 10D, could be used to supply the unit cell's IC chip with the necessary electrical signal to determine the plunger's position via the line labeled 'S'. With the ability to actuate and sense the position of each sector's plunger, the lattice's unit cells can independently control their interactions using closed-loop control as governed by the instructions uploaded within each unit cell's IC chip. Note from the cross-sectional view of each unit cell in Figure 10E that a large percentage of the design's volume is afforded to the IC chips as well as potential antennas, if wireless uploading of control instructions is desired, and/or batteries, if the material is intended to operate in the absence of an external power source. If such batteries are also rechargeable, the lattice could be recharged by cyclically loading the material's lattice externally because the design's piezo actuators would reversibly generate electrical power as they are mechanically strained. And, although it may be possible to actively control the lattice

such that it exhibits isotropic material properties, the geometry of each unit cell possesses the necessary nine planes of symmetry [76] to passively exhibit cubic material properties.

The proposed material would require advanced additive fabrication processes to realize. Such processes would require the ability to print true-3D high-resolution features made of three different materials—piezo materials for the actuators, conductive materials for electrical wiring, and non-conductive materials for the general structure. Once half a layer of cells is printed using these materials, a robotic arm could then be used to simultaneously insert and wire bond the IC chips, antennas, and/or batteries inside the cells' center. Then the additive process could resume to complete the layer of cells and begin another layer. After many such iterations, the material could be realized as proposed. Although this and other potential fabrication approaches will generate imperfect or faulty features within the proposed lattice, it is important to recognize that the proposed design's unit cells consist of many redundant flexures and electrical wires to accommodate such flaws. Additionally, since so many unit cells constitute a typical lattice, the overall bulk material response will be largely unaffected even if sizable numbers of entire unit cells don't function properly.

4.1.2 Modeling and Optimization

To analyze the performance of the proposed design, we first establish an analytical model for calculating the proposed design's maximum achievable positive and negative strains and the maximum tensile and compressive forces that the design can resist without causing any of its elements to yield, buckle, or collide.

Each unit cell's sector is modeled as Euler beam elements that join together at rigid nodes, shown dark grey in Figure 11A. Note that the beam elements in the design of Figure 11A are labeled 'Silicon' and 'Piezo (PZT-5H).' An equation that can be used to calculate the displacements and rotations of this design's unfixed rigid nodes that result from the piezo actuators being subject to a change in electric field, ΔE, is

$$\begin{bmatrix} \mathbf{T_1} & \mathbf{T_2} & \cdots & \mathbf{T_R} \end{bmatrix}^T = -[K]^{-1}\mathbf{A}\Delta E, \tag{4.1}$$

where $\mathbf{T_b}$ are 1×6 displacement twist vectors that contain the necessary information to determine the displacements and rotations of the unfixed rigid nodes assigned the number b. Note that R is the total number of unfixed rigid nodes in the design. Instructions for constructing the [K] matrix and **A** vector in Equation (4.1) for general flexible structures are provided in [45]. Once the piezo-actuated displacements and rotations of each unfixed rigid node in the structure are known, the theory discussed in [45] can be used to calculate the three forces, f_1, f_2, and f_3, and three moments, Γ_1, Γ_2, and Γ_3, acting along and about orthogonal axes at one end of each beam element in the structure as if they were held fixed at their opposing end.

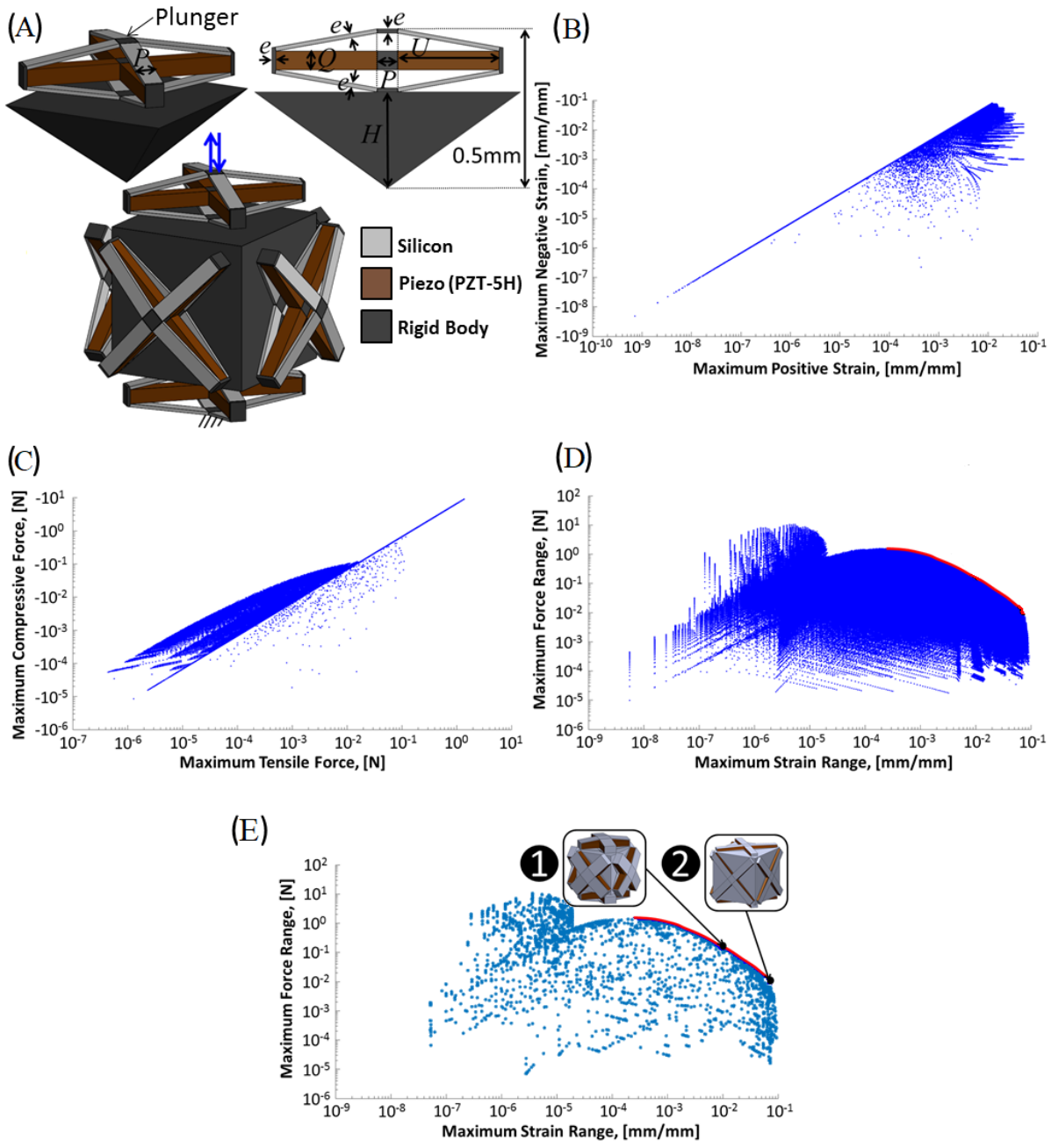

Figure 11: Simplified unit cell topology defined by five independent parameters (A), maximum positive vs. negative strains for every design instantiation (B), maximum tensile vs. compressive forces (C), maximum strain vs. force ranges (D), maximum strain vs. force ranges result generated using the computational optimization tool introduced in Chapter 3 (E)

The Mises stress at select locations within each beam element can be calculated according to

$$\sigma_{Mises}(x,y,z)=\sqrt{\sigma_{33}^2+3\left(\sigma_{13}^2+\sigma_{23}^2\right)}, \tag{4.2}$$

where

$$\sigma_{33}=\frac{f_3}{wt}-\frac{12f_1x(L-z)}{tw^3}-\frac{12f_2y(L-z)}{wt^3}+\frac{12\Gamma_1y}{wt^3}-\frac{12\Gamma_2x}{tw^3}, \tag{4.3}$$

and w, t, and L are the beam element's width, thickness and length labeled in Figure 12A. If $w \geq t$, σ_{13} and σ_{23} from Equation (4.2) are

$$\sigma_{13}=\frac{6f_1}{tw^3}\left(\left(\frac{w}{2}\right)^2-x^2\right)-\left(\frac{8w\Gamma_3}{J\pi^2}\sum_{n=1,3,5}^{\infty}\frac{(-1)^{(n-1)/2}\cos\left(\frac{n\pi x}{w}\right)\sinh\left(\frac{n\pi y}{w}\right)}{n^2\cosh\left(\frac{n\pi t}{2w}\right)}\right), \tag{4.4}$$

where

$$J=\frac{t^3w}{3}\left(1-\frac{192t}{\pi^5w}\sum_{n=1,3,5}^{\infty}\frac{1}{n^5}\tanh\left(\frac{n\pi w}{2t}\right)\right), \tag{4.5}$$

and

$$\sigma_{23} = \frac{6 f_2}{w t^3}\left(\left(\frac{t}{2}\right)^2 - y^2\right) + \left(\frac{2\Gamma_3 x}{J} - \frac{8 w \Gamma_3}{J\pi^2}\sum_{n=1,3,5}^{\infty}\frac{(-1)^{(n-1)/2}\sin\left(\frac{n\pi x}{w}\right)\cosh\left(\frac{n\pi y}{w}\right)}{n^2\cosh\left(\frac{n\pi t}{2w}\right)}\right). \quad (4.6)$$

If $w<t$, σ_{13} and σ_{23} from Equation (4.2) are

$$\sigma_{13} = \frac{6 f_1}{t w^3}\left(\left(\frac{w}{2}\right)^2 - x^2\right) + \left(-\frac{2\Gamma_3 y}{J} + \frac{8 t \Gamma_3}{J\pi^2}\sum_{n=1,3,5}^{\infty}\frac{(-1)^{(n-1)/2}\sin\left(\frac{n\pi y}{t}\right)\cosh\left(-\frac{n\pi x}{t}\right)}{n^2\cosh\left(\frac{n\pi w}{2t}\right)}\right), \quad (4.7)$$

where

$$J = \frac{w^3 t}{3}\left(1 - \frac{192 w}{\pi^5 t}\sum_{n=1,3,5}^{\infty}\frac{1}{n^5}\tanh\left(\frac{n\pi t}{2w}\right)\right), \quad (4.8)$$

and

$$\sigma_{23} = \frac{6 f_2}{w t^3}\left(\left(\frac{t}{2}\right)^2 - y^2\right) - \left(\frac{8 t \Gamma_3}{J\pi^2}\sum_{n=1,3,5}^{\infty}\frac{(-1)^{(n-1)/2}\cos\left(\frac{n\pi y}{t}\right)\sinh\left(-\frac{n\pi x}{t}\right)}{n^2\cosh\left(\frac{n\pi w}{2t}\right)}\right). \quad (4.9)$$

For each beam element, the Mises stress in Equation (4.2) will be the largest at one of nine locations, shown as black dots in Figure 12B, at either end of the beam element (i.e., 18 total locations per beam element). Once the Mises stress at these 18 locations are calculated for every beam element in the piezo-actuated structure, designers can know if the structure has failed due to yielding if any of these Mises stresses exceed the yield strength of their corresponding beam elements.

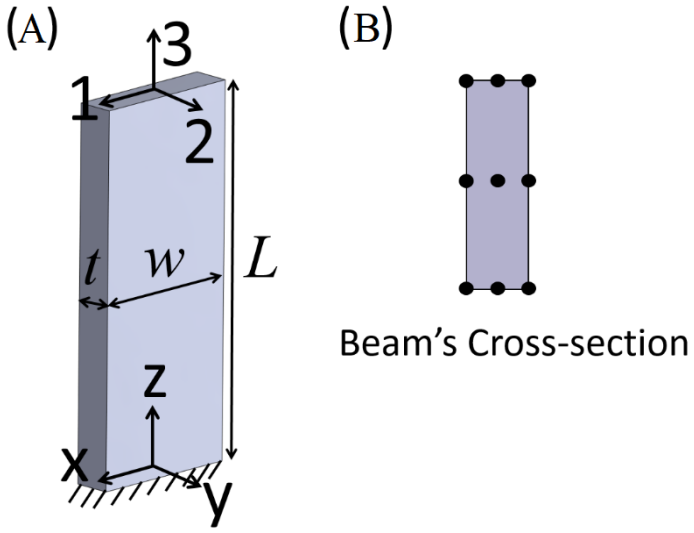

Figure 12: A general beam element with labeled parameters and coordinate axes that establish this paper's mathematical convention (A), and a cross-section of the beam element showing the nine locations at which the Mises stress is calculated at its top and bottom ends to determine if the deformed beam has yielded (B).

Similarly, the internal axial forces, f_3, within each beam element can be used to determine if the piezo-actuated structure has failed due to buckling if f_3 is negative (i.e., a compressive force) and its magnitude exceeds $F_{critical}$, which can be calculated according to

$$F_{critical} = \frac{E\pi^2 wt^3}{3L^2}, \tag{4.10}$$

when w≥t. If, however, t<w, $F_{critical}$ can be calculated according to

$$F_{critical} = \frac{E\pi^2 tw^3}{3L^2}. \tag{4.11}$$

In addition to making sure no beam elements within the unit cell yield or buckle for a given piezo-actuated scenario, it is also important to mathematically ensure that the corner rigid nodes of the transmission mechanisms at the far ends of the piezo actuators don't collide with other similar neighboring nodes within the unit cell when the piezo actuators extend. Enforcing this condition can be done by tracking the relative displacements and rotations of these rigid nodes for a given change in electric field using Equation (4.1).

Thus, for a given design instantiation, the maximum achievable strain can be calculated by fixing the pyramid-shaped rigid body in the sector topology shown dark grey in Figure 11A, and applying the piezo actuators minimum electric field value in Equation (4.1) to calculate the resulting $\mathbf{T_1}$ through $\mathbf{T_6}$ displacement twist vectors of the six unfixed rigid nodes when the piezo

actuator contracts it's largest allowable amount. If the resulting displacements and rotations of these six nodes do not cause any of the failure conditions (i.e., beam elements that yield or buckle, or transmission mechanism corner nodes that collide), the upward displacement of the node labeled 'Plunger' in Figure 11A can be divided by the sector height (i.e., 0.5mm) to determine the maximum achievable positive strain of the overall lattice. If, however, the failure conditions do occur using the piezo actuator's minimum electric field value, this value can be divided in half and reapplied to Equation (4.1). By iteratively adding or subtracting similar half increments to the attempted electric field value, the smallest value can be identified that will produce the largest positive lattice strain without causing any yielding, buckling, or colliding of the sector's elements. The same process can also be applied to find the lattice's maximum negative strain by starting with the maximum electric field and using the same iterative process to identify the largest electric field that causes the piezo actuators to expand without violating the failure conditions. The resulting downward displacement of the plunger divided by the sectors height will be the maximum achievable negative strain of the lattice.

The maximum compressive force that a single unit cell can resist by contracting its piezo actuators such that its plunger does not move can also be calculated by fixing both the pyramid-shaped rigid body and the plunger node in the sector shown in Figure 11A, and applying the piezo actuators minimum electric field value in Equation (4.1) to calculate the resulting $\mathbf{T}_1$ through $\mathbf{T}_5$ displacement twist vectors of the remaining five unfixed rigid nodes when the piezo actuator contracts it's largest allowable amount. If the resulting displacements and rotations of these five nodes do not cause any of the failure conditions (i.e., beam elements that yield or buckle, or transmission mechanism corner nodes that collide), the net internal force imparted on the fixed

plunger can be calculated and its sign reversed to determine the maximum compressive force that the single unit cell can resist with infinite stiffness. If, however, the failure conditions do occur using the piezo actuator's minimum electric field value, this value can be divided in half and reapplied to Equation (4.1) in the same iterative fashion described previously until the smallest electric field value can be identified that will cause a single cell to resist the largest compressive force possible without causing any yielding, buckling, or colliding of the sector's elements. Again the same process can be repeated using the maximum electric field to determine the maximum tensile force that a single unit cell can resist with infinite stiffness by extending its piezo actuators such that its plunger remains fixed without causing any yielding, buckling, or colliding of elements.

To determine what ranges of properties the design topology can achieve, its geometry is simplified such that it can be defined by five independent parameters labeled in Figure 11A (i.e., *P*, *Q*, *H*, *e*, and *U*). Suppose the beams labeled 'Silicon' in Figure 11A possess a Young's modulus of 190GPa, a shear modulus of 75GPa, and a yield strength of 7GPa. Suppose also the piezo actuator beams, labeled 'Piezo (PZT-5H)', possess a Young's modulus of 43GPa, a shear modulus of 16GPa, a yield strength of 76MPa, a maximum electric field of 2kV/mm, a minimum electric field of -0.3kV/mm, and an axial charge constant of 0.64nm/V. For a 1mm-sized unit cell, the maximum positive and negative strain values the lattice can achieve are plotted in Figure 11B for almost one million different design instantiations. These design instantiations, shown as individual blue dots in Figure 11B, were generated by conducting a sweep of all the independent design parameters starting from a smallest allowable feature size (i.e., 1μm) and incrementing each parameter small amounts until the largest geometrically compatible feature sizes were reached. The maximum and minimum strain values were determined by calculating the largest distance the

top face of the plunger could be displaced by the piezo actuators up and down without causing any elements within the sector to yield, buckle, or collide, and then divide these displacements by the sector height (i.e., 0.5mm). The maximum compressive and tensile forces, shown as blue arrows in Figure 11A, that can be resisted by the piezo actuators of a 1mm-sized unit cell such that its plunger does not move without causing any elements within the sector to yield, buckle, or collide are plotted in Figure 11C for the same design instantiations plotted in Figure 11B. They are significant because they represent the ranges of loading forces between which the cell could be programmed to respond with any stiffness. Note that these cells could still achieve a programmable stiffness if they were loaded with forces outside of this range, but the resulting ranges of achievable stiffness would be reduced to finite ranges. Note also that although the strains plotted in Figure 11B are independent of the unit cell's scale factor, s (i.e., size), the forces plotted in Figure 11C scale by a factor of s^2. Note that the plot of Figure 11C was generated with a scale factor of one (i.e., a 1mm-sized unit cell). Optimal design instantiations can be identified by plotting the maximum force ranges (i.e., the maximum compressive forces subtracted from the maximum tensile forces of Figure 11C) against the maximum strain ranges (i.e., the maximum negative strains subtracted from the maximum positive strains of Figure 11B) as shown in Figure 11D. The computational tool introduced in Chapter 3 was used to generate Figure 11E, which is the same plot as Figure 11D except that the computational tool only need to evaluate 2508 different input combinations to generate the full boundary, instead of near one million evaluations in Figure 11D.

The optimal design instantiations with the largest ranges of maximum forces and maximum strains lie along the curve shown red in Figure 11D and E. Two sample designs from this curve are labeled (1) and (2) in Figure 11E. Their predicted performance calculated via the analytical

method of this paper is provided in Table 1 and Table 2 respectively. This performance was verified using finite element analysis as provided in the same tables. Note that the design with larger junction nodes (i.e., design 1) possesses more error because of the analytical method's rigid body assumption.

Table 1: Finite element verification of the analytical predictions pertaining to design 1 from Figure 11E with P=0.190mm, Q=0.090mm, H=0.310mm, e=0.011mm, and U=0.290mm

	Analytical Calculations	Finite Element Results	Percent Error
Maximum Positive Strain	0.14%	0.15%	6.67%
Maximum Negative Strain	-0.95%	-1.05%	9.52%
Maximum Tensile Force	0.129N	0.121N	6.61%

Table 2: Finite element verification of the analytical predictions pertaining to design 2 from Figure 11E with P=0.120mm, Q=0.040mm, H=0.420mm, e=0.004mm, and U=0.470mm

	Analytical Calculations	Finite Element Results	Percent Error
Maximum Positive Strain	0.95%	0.99%	4.04%
Maximum Negative Strain	-6.28%	-6.58%	4.56%
Maximum Tensile Force	0.00843N	0.00827N	1.93%

4.2 An Electrothermal-actuated Microarchitectured Material

4.2.1 Design

The active microarchitectured material introduced in this section (Figure 13) consists of a large periodic lattice of 5mm-sized cubic cells. Each cell is actuated by electrothermal actuators that are independently controlled to push (extend in the longitudinal direction) or pull (contract in the longitudinal direction). Similar to the active microarchitectured material introduces in Section 4.1, this material exhibits desired combinations bulk mechanical properties according to control instructions.

The periodic lattice of unit cells is shown in Figure 13A. Each unit consists of six identical electrothermal actuators (Figure 13B and C) that are attached to the six sides of a center cube. The length of each actuator is designed to be 5mm such that the overall size of each unit cell assembly is 5mm. The lattice's unit cells are joined together at the contact interfaces (labeled in Figure 13B) such that all unit cells in the lattice share the same the power source and electrical ground. A microprocessor is placed inside the center cube that provides power and control instructions to each actuator through the gold contacts, i.e., the yellow areas on the sides of the green center cube in Figure 13B. Each actuator is designed with two electrothermal loops (labeled as yellow and orange arrows in Figure 13D) that are mechanically attached but electrically insulated. During the actuation, the current flow is directed through the gold traces to the targeted joule heating components in either electrothermal loops. When a current i_{push} is applied to the outer current loop, as indicated by the yellow arrow in Figure 13D, the temperature of the parallel beams in the outer loop will increase rapidly due to Joule heating effect. The transmission structure of the actuator is designed such that the thermal expansion of the beams in the outer loop is constrained in the

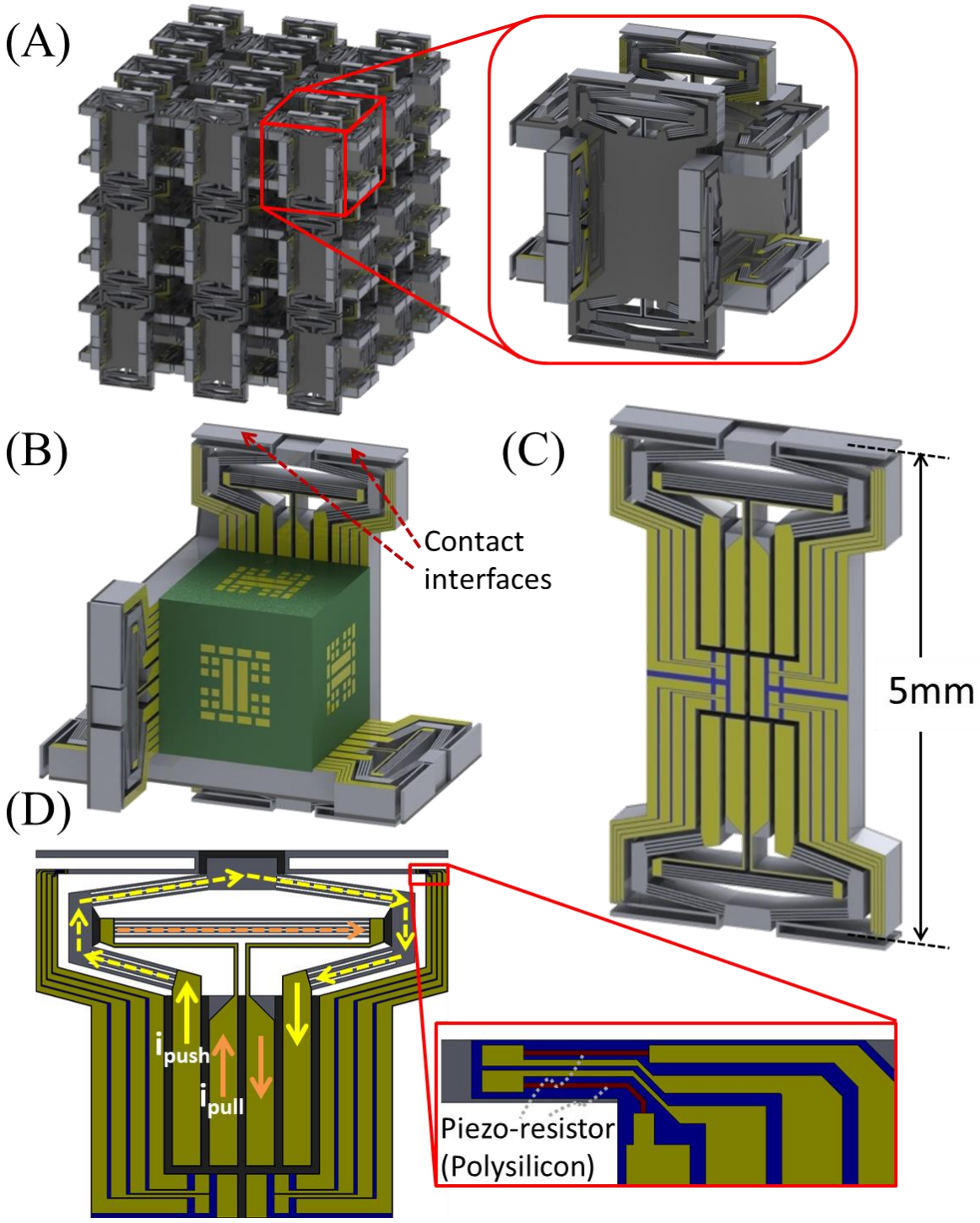

Figure 13: Active microarchitectured material lattice design (A), the center cube exposed by removing the actuators on three sides (B), the electrothermal actuator design (C) and (D)

horizontal direction by the parallel beams in the inner loop. As a result, the small thermal expansion along the beams is amplified and converted to an upward vertical motion of the contact interfaces. Similarly, when the current i_{pull} is applied to the inner current loop (labeled with the orange arrow in Figure 13D), the Joule heating of the parallel beams in the inner loop results in a downward vertical motion of the contact interfaces. To precisely measure and control the displacement of each actuator, piezo-resistive (polysilicon) strain gauges are attached to the microstructure at the location shown in Figure 13D, where the maximum strain is most likely to occur for both actuation directions (pushing and pulling). The strain gauges are connected to the microprocessor at the center of each unit cell through the gold traces shown in yellow in Figure 13D.

Each actuator was fabricated separately and assembled onto the center cube. The thermal actuator is designed to be fabricated on a silicon-on-insulator (SOI) wafer. The electrothermal beams were fabricated by selectively etching the device layer (silicon) as shown in Figure 14A. The structure on the handle layer (silicon) was etched as shown in Figure 14B and it is electrically and thermally insulated from the device layer by the buried oxide (BOX) layer in between. It provides the necessary mechanical connections between the two electrothermal loops on the device layer to constrain their motion. A layer of non-conductive silicon nitride was deposited, patterned and etched on the top of the device layer to insulate the device layer from the gold traces as shown in Figure 14C. A polysilicon layer was deposited on top of the silicon nitride, and the strain gauges were etched as shown in Figure 14D. The gold traces were deposited as the top layer of the device, which establishes electrical connections between the micro-actuator and external circuits. The

microfabrication process flow is shown in Figure 15. The fabricated devices are shown in Figure 16.

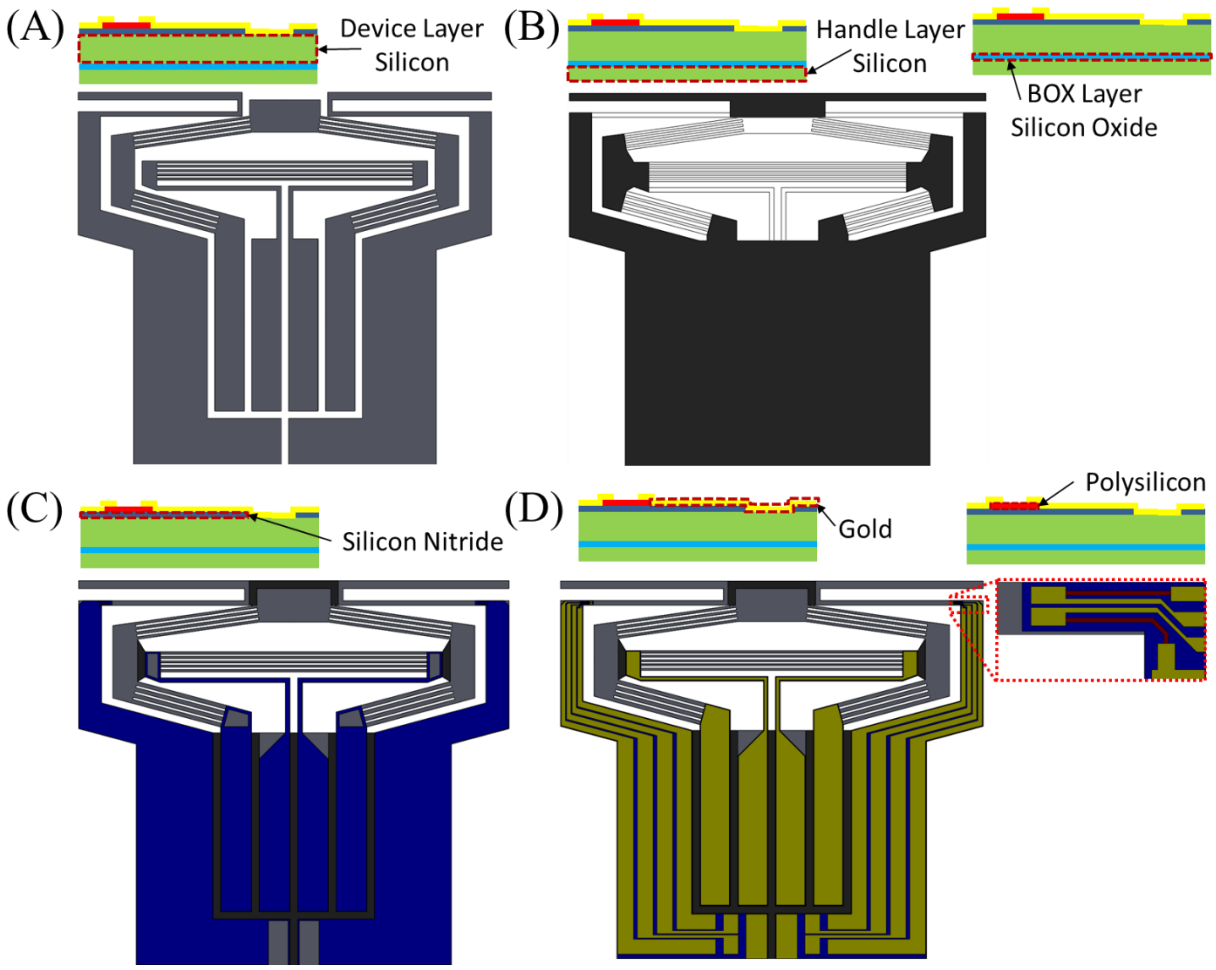

Figure 14: Electrothermal actuator's device layer (A), handle and buried oxide layer (B), silicon nitride insulation layer (C), and gold and polysilicon layer (D)

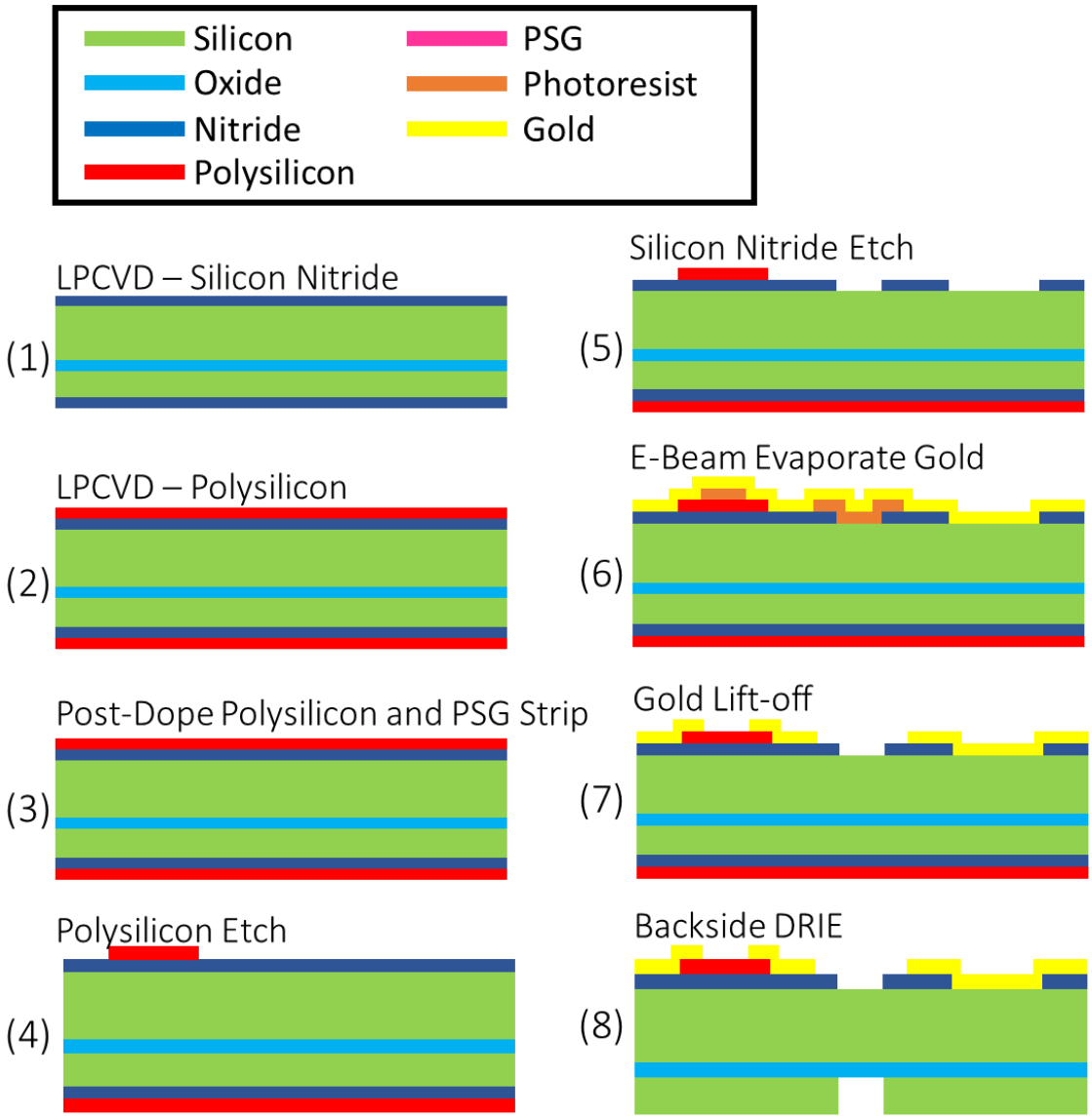

Figure 15: Electrothermal actuator microfabrication process flow

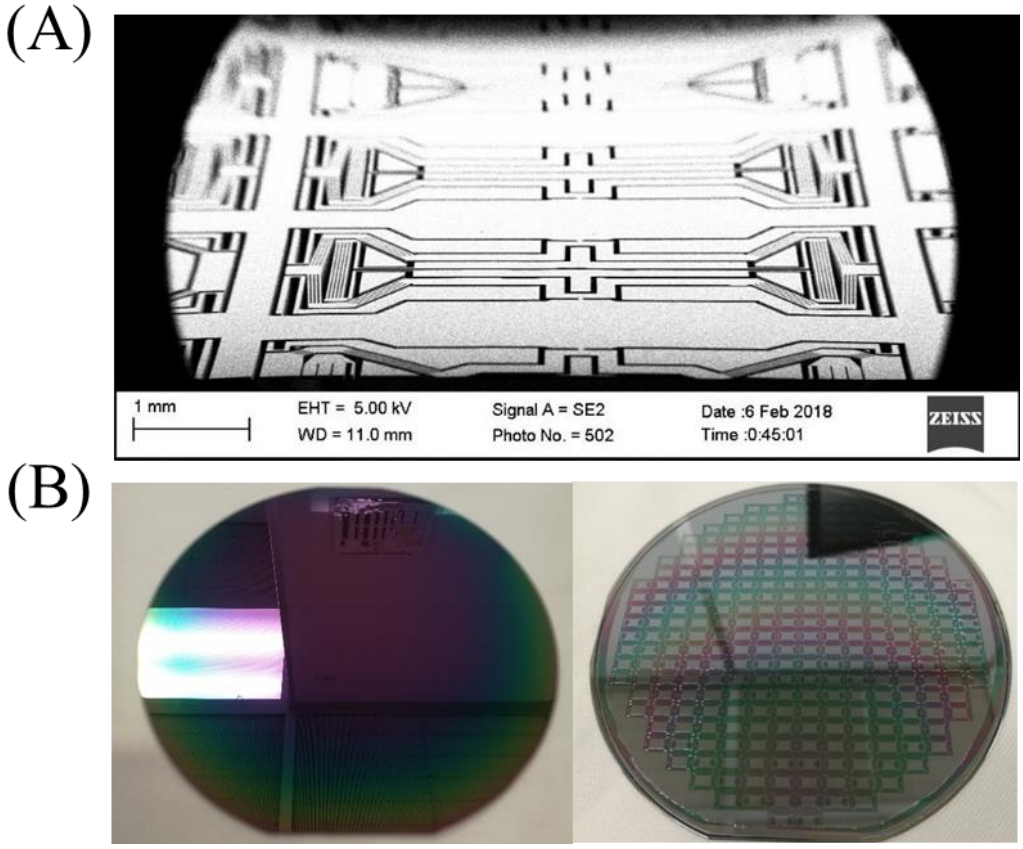

Figure 16: Photo of the fabricated electrothermal actuator (A), SOI wafer before and after microfabrication (B)

4.2.2 Modeling and Optimization

To analyze the performance of the electrothermal-actuated metamaterial, the geometry of the actuator is simplified such that it can be defined by eleven independent parameters labeled in Figure 17 and listed in Table 3. Every combination of the eleven parameters uniquely determines a thermal actuator design. An automatic tool was developed that generates the complete CAD model and calculates the FEA result according to a given set of design parameters. The material properties used in the FEA is shown in Table 4. The FEA model produces the maximum force and

displacement of a given design by applying the maximum allowable voltage on the inner and out electrothermal loop of the actuator respectively. The maximum allowable voltage is derived under the following conditions: *1)* No beams yield or buckle, and *2)* the maximum temperature of the device is lower than 750 ℃.

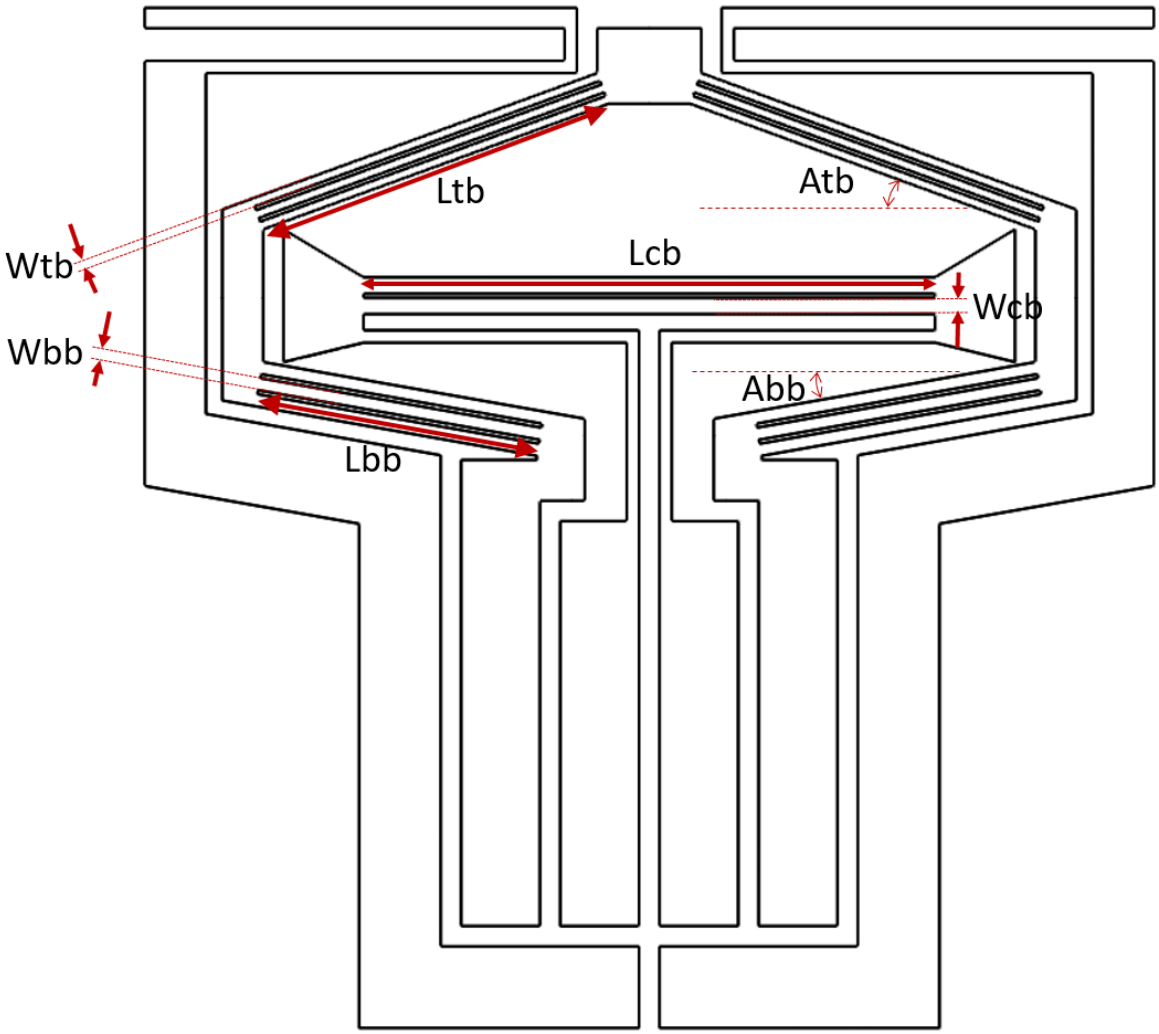

Figure 17: Simplified thermal actuator design topology defined by eleven independent parameters

Table 3: Design parameters and their range

Parameter name	Description	Unit	Range
Ncb	Number of the center beams		[1, 25]
Lcb	Length of the center beams	mm	[0.1, 2.5]
Wcb	Width of a center beam	mm	[0.02, 0.1]
Abb	Angle of the bottom beams	Degree	[1, 45]
Nbb	Number of the bottom beams		[1, 25]
Lbb	Length of the bottom beams	mm	[0.1, 2.5]
Wbb	Width of a bottom beam	mm	[0.02, 0.1]
Atb	Angle of the top beams	Degree	[1, 45]
Ntb	Number of the top beams		[1, 25]
Ltb	Length of the top beams	mm	[0.1, 2.5]
Wtb	Width of a top beam	mm	[0.02, 0.1]

Table 4: FEA Material Properties

Material Property		Gold	Silicon Dioxide	Silicon
Density	kg/m^3	19300	2270	2330
Coefficient of Thermal Expansion	1/C	1.42×10^{-5}	5.00×10^{-7}	$2.57\times10^{-6*}$
Young's Modulus	GPa	79.0	70	166
Poisson's Ratio		0.44	0.17	0.28
Thermal Conductivity	W/(m·C)	31	1.4	148
Resistivity	Ohm·m	2.19×10^{-8}	1×10^{17}	0.05
Tensile Yield Strength	MPa		155	166
Compression Yield Strength	MPa		1500	3200

* The value is shown only for room temperature. In the FEA model, the coefficient of thermal expansion of silicon is set to be a function of the temperature according to the empirical equation provided in [77].

To determine what ranges of performance capabilities the design topology can achieve, we utilized the computational tool introduced in Chapter 3 in conjunction with the FEA model and produced the result shown in Figure 18, where the maximum stress range is plotted against the maximum strain range (defined in Section 4.1.2) for a 5mm cube. In total, 5630 designs are evaluated and plotted. Two sample designs on the optimal design curve (shown in red) are labeled (1) and (2) in Figure 18.

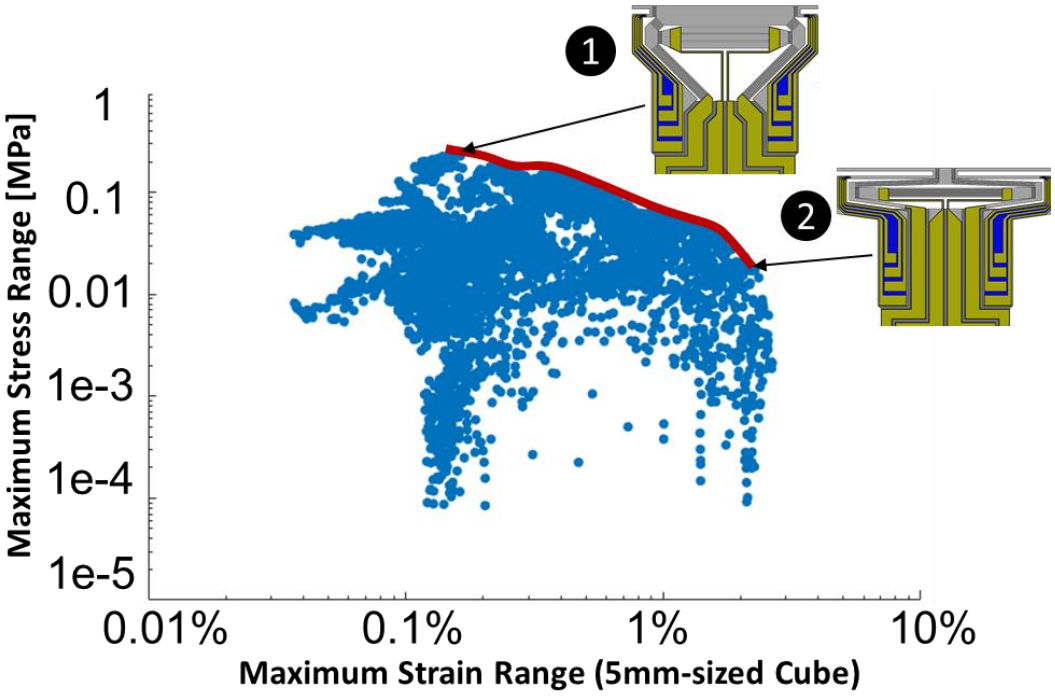

Figure 18: Maximum strain vs. force ranges result generated using the computational optimization tool introduced in Chapter 3

Chapter 5:

Conclusion

In this dissertation, we propose a design paradigm that helps the designers to create new types of active microarchitectured materials. General guidelines are provided for designing active microarchitectured metamaterials. The principles for optimally placing the actuator are established by extending the FACT theory. Different types of actuation have been reviewed and compared from the perspective of active metamaterial design to help designers select the proper ways for actuation. An automatic computational tool is created for identifying the boundary of the design space and obtaining the optimal design parameters.

5.1 Recommended Future Work

The research of active microarchitectured metamaterials is still in its early stage, and there are a few key challenges that future research efforts need to address. First, the fabrication of active microarchitectured metamaterial is largely limited by the current micro-fabrication and micro-manipulation techniques. In order to enable the fabrication of active metamaterials, advanced additive fabrication processes need to be developed that are capable of producing three-dimensional multi-material microstructures with high throughput. Secondly, modeling and analysis of the metamaterial as a large lattice of unit cells rely heavily on traditional FEA algorithm, which often requires a massive amount of calculation. New algorithms and computational tools need to be developed that analyze the metamaterial performances more efficiently by exploiting

the periodicity of metamaterials. Lastly, advanced control algorithms need to be developed for active metamaterials such that an overall desired behavior (i.e., a bulk property) emerges from the interactions of the unit cells that are programmed to obey simple instructions relating to the behavior of the other unit cells.

Appendix A: MMA Performance Metrics

In this section, MMA performance metrics (e.g., individual mirror area, fill factor, array pitch, range of motion, maximum acceleration, actuator energy density, and number of uncontrolled DOFs within each mirror system's flexure bearings) are standardized using definitions that can be applied to general MMA designs to enable fair comparisons. To highlight why it is difficult to compare the performance capabilities of existing MMA designs using the currently unstandardized metric definitions, consider the following simple example. Suppose the micromirror of a particular MMA could be actuated to tip in one direction from its passive equilibrium position by 3mrad and could be actuated to tip in the other direction by another 3mrad from the same equilibrium position. Some papers may define the mirror's range to be the range from the equilibrium position (i.e., 3mrad). Other papers may define the range to be the total range over which the mirror can move (i.e., 6mrad). Still other papers may define the range to be the optical range (i.e., the full range over which light can be reflected), which would be twice the total mirror range (i.e., 12mrad). It would not be consistent to compare the motion range of different designs if each design's range was defined using different definitions. Thus, this section standardizes the definitions of multiple performance metrics of interest to MMA technologies and applies them to existing designs so they can be fairly compared.

A.1 Mirror Area, Fill Factor, and Pitch

This section standardizes the definitions of three related metrics—mirror area, fill factor, and pitch. Although these three metrics pertain to the geometry of MMA designs, we treat them as

performance metrics since they strongly affect the performance capabilities of MMA designs and are typical specified as functional requirements by MMA designers.

Mirror area, A_m, is a metric that provides designers with a sense of the size of each repeating mirror element within the periodic array. For designs with discrete mirror surfaces, this area is the reflective area intended for directing light on the surface of a single mirror element within the array. For continuous mirror surfaces, the mirror-area metric is the area occupied by each individual mirror system repeated within the array.

There are two kinds of fill factor metrics documented in the MMA design database in Supplemental Materials—reflected fill factor and directed fill factor. Reflected fill factor is the percent of the area that reflects light from the surface of each mirror system within the array. Directed fill factor is the percent of the area that reflects light from only the reflective portion of the mirror element of each mirror system within the array. When we refer to a design's fill factor, γ_F, without specifying whether it is the reflected or directed type, directed fill factor is what is meant. The only exception to this rule is that for continuous-mirror-surface designs, their fill factor is always defined to be 100% since the entire surface of such designs reflects all the light that hits it, even though not all the reflected light can be controlled or directed as completely desired. This inability to direct all the reflected light is due to the fact that the surface of each mirror element within continuous designs is connected to and thus partially deformed by its neighbors, which may be attempting to point their mirror elements in different directions. Since, however the true directed fill factor of continuous designs is difficult to calculate and changes depending on how each mirror element is actuated within the array, both the directed and reflected fill factor of all continuous designs is generously set to 100%.

The pitch, L, of an MMA is defined as the square root of the area occupied by each individual mirror system repeated within the array. The pitch metric provides designers with a sense of the average distance between the centers of each neighboring mirror element whether the design is discrete or continuous. Note that for 2D arrays, the distance between neighboring mirror elements may be different in different directions (e.g., the distance in the x-direction may be shorter than in the y-direction for rectangular mirrors). Note that according to the standardized definitions of the geometry metrics introduced in this section, an MMA design's mirror area, A_m, its fill factor, γ_F, and its pitch, L, are related according to

$$A_m = \gamma_F L^2 . \tag{A.1}$$

A.2 Range of Motion

This section standardizes the definitions of various ranges of motion metrics as they apply to general MMA designs. Equilibrium and full range of motion are defined and applied to discrete and continuous mirror-surface designs for their rotational (i.e., tip and tilt) DOFs.

The rotational equilibrium range of motion of an MMA design's tip or tilt DOF, θ_{eq}, is the maximum angle over which the system's mirror elements can each be rotated from their passive or actuation load-free equilibrium position to an extreme orientation in either direction (i.e., clockwise or counter clockwise) such that the mirror element can be statically held in place in that stable orientation. Note that some MMA designs can tip more than they can tilt or vice versa. Thus, the rotational equilibrium range of motion of a general MMA design is generously chosen to

correspond with the rotational DOF that can achieve the larger angular displacement from the equilibrium position.

The rotational full range of motion of an MMA design's tip or tilt DOF, θ_{full}, is the sum of the angle over which the system's mirror elements can each be rotated from their equilibrium position to one extreme orientation in the clockwise direction, and the angle over which the elements can be rotated from their equilibrium position to another extreme orientation in the counter clockwise direction. For design's that achieve both tip and tilt DOFs, the rotational full range of motion of an MMA design is also generously chosen to correspond with the rotational DOF that can achieve the larger angular displacement sum.

Note that for most MMA designs (particularly for symmetric designs or designs with bipolar actuators) the full range of motion is often twice the equilibrium range of motion (i.e., $d_{full}=2d_{eq}$ and $\theta_{full}=2\theta_{eq}$) although this is not a hard assumption for translational or rotational DOFs. Note that some designs can move their mirror elements over a larger range of motion in one direction from the equilibrium position than they can move their elements in the other direction. For such cases, the larger of the two ranges of motion from the equilibrium position is defined as the system's equilibrium range of motion. Note also that for some MMA designs with unipolar actuators, the full range of motion is often equal to the equilibrium range of motion.

A.3 Maximum Acceleration

This section standardizes the definition of the maximum acceleration achieved by general MMA designs about their rotational (i.e., tip and tilt) DOFs. The definition does not apply to designs that utilize the digital actuation approach because such designs rely on mechanical hard stops that abruptly decelerate the mirrors to achieve their intended pointing orientations via

collisions and thus their pointing behavior cannot be modeled using traditional second-order mass-spring analysis.

The maximum angular acceleration, α_{max}, that the mirror elements of such designs can achieve either about their tip or tilt DOF during operation is defined as

$$\alpha_{max} = \left(2\pi \cdot f_{\theta n}\right)^2 \theta_{eq,f} \gamma_{\theta}, \tag{A.2}$$

where $f_{\theta n}$ is the higher of the two natural frequencies that correspond to either the mirror's tip or tilt DOF mode shapes in units of Hertz. The range of motion $\theta_{eq,f}$ is the maximum angle in radians over which the design's mirror elements can be rotated about the axis of the DOF mode shape corresponding to $f_{\theta n}$ from each mirror element's equilibrium position to the orientation where they can be statically held in place by the system's actuators. Note that an MMA design's $\theta_{eq,f}$ is not always equal to its θ_{eq} if the design possesses both a tip and a tilt DOF. An MMA design, for example, may possess a tip-DOF mode shape that corresponds with a higher natural frequency than the natural frequency corresponding to its tilt-DOF mode shape, but the system's mirror element may be able to be rotated about its tilt DOF with a larger angular range than its mirror element could be rotated about its tip DOF from its equilibrium position. θ_{eq} is always the larger of the two rotational ranges of motion about either the tip or tilt DOFs. The angular overdrive ratio, γ_{θ}, is defined as

$$\gamma_\theta = \frac{\tau_{max}}{\tau_{max\theta}}, \tag{A.3}$$

where τ_{max} is the maximum moment that can be applied to the design's mirror element by the system's actuators about the tip or tilt DOF corresponding to the mode shape of $f_{\theta n}$, and $\tau_{max\theta}$ is the moment required to rotate the mirror element by $\theta_{eq,f}$ about its corresponding tip or tilt DOF axis. Although for most MMA designs γ_θ =1, some designs possess actuators that can impart a larger moment on their mirror elements than is necessary to rotate the mirror elements to their maximum pointing orientations where their flexures either come close to yielding, buckling, or causing the systems' rigid bodies to collide (i.e., γ_θ >1).

A.4 Actuator Energy Density

This section introduces a standardized definition of the energy density of the actuators within general MMA designs for both their rotational (i.e., tip and tilt) DOFs. This definition provides a normalized metric for fairly comparing the power of each MMA design's actuators regardless of the size of their mirror elements.

The actuator angular energy density of MMA designs pertaining to their tip or tilt DOFs, $U_{\theta max}$, is given by

$$U_{\theta max} = \frac{E_{\theta max}}{L^3}, \tag{A.4}$$

where $E_{\theta max}$ is the maximum energy that can be imparted from the MMA designs' actuators to their mirror elements to cause them to rotate, and L is the pitch of the MMA designs. The maximum energy available for dynamics, $E_{\theta max}$, is given by

$$E_{\theta max} = \frac{1}{2} J \alpha_{max} \theta_{eq,f}, \tag{A.5}$$

where J is the rotational moment of inertia that captures the system's full inertia as its mirror element rotates about the applicable tip or tilt axis. It was calculated for each MMA design using

$$J = C_1 A_m m, \tag{A.6}$$

where C_1 is a scalar coefficient that depends on the shape of the mirror element (e.g., C_1=1/12 for a square mirror), and m is the mirror element's mass defined by

$$m = C_2 \rho_m A_m^{3/2}, \tag{A.7}$$

where C_2 is the aspect ratio between the mirror element's thickness and its characteristic length (i.e., $A_m^{1/2}$), and ρ_m is the density of the mirror element. Since an accurate C_1 coefficient was difficult to determine for many of the MMA designs in the literature, C_1 was set to the typical value of 1/12 for every design reviewed for this paper regardless of their actual mirror shape.

Similarly, the C_2 aspect ratios for all designs reviewed were all set to 10^{-2}, which is a typical value for most designs.

Appendix B: Actuator Energy Density Limits

This section provides the equations and assumptions used to plot the actuator energy density performance limits represented by the colored dashed lines in Figure 7 of Section 2.3 for each type of MMA actuator. These limits were derived for MMA designs that achieve at least tip and a tilt DOFs (e.g., TT and TTP designs) and represent the theoretical upper bounds on the performance of such designs. The details of the derivation are provided in [27]. Although unlikely, it may be possible for future MMA designs to achieve or even slightly surpass the derived performance limits of this section if clever tricks are implemented within their design that invalidate some of the assumptions used to derive the limits.

B.1 Plate Actuators

B.1.1 Performance Limit Equation

The angular energy density limit of general MMA designs that achieve at least tip and tilt DOFs using plate actuators, $U_{\theta plate}$, is defined as

$$U_{\theta plate} = \frac{\varepsilon_r \varepsilon_0 V_{max}^2 \theta_{full}}{4 d_{plate}^2} \gamma_L \gamma_A , \tag{B.1}$$

where ε_r is the relative permittivity, ε_0 is the absolute permittivity of free space and equals 8.85×10^{-12}F/m, V_{max} is the maximum voltage that can be applied to the actuators, θ_{full} is the

system's rotational full range of motion (defined in Appendix A), and d_{plate} is the gap distance between the actuators' plates. The lever ratio, γ_L, is defined as

$$\gamma_L = \frac{L_{lever}}{L}, \tag{B.2}$$

where L_{lever} is the shortest distance from the axis of the rotational DOF to the location where the actuators impart their effective point force on the mirror element (i.e., L_{lever} is the lever arm length), and L is the system's pitch defined in Appendix A. The actuator-area ratio, γ_A, is defined as

$$\gamma_A = \frac{A_{act}}{L^2}, \tag{B.3}$$

where A_{act} is the total actuator area that can be used to drive the rotational DOF.

B.1.2 Assumptions Used to Simply the Performance Limit Equation

The angular energy density performance limits of plate-actuated MMA designs, $U_{\theta plate}$, plotted as the dashed red lines in Figure 7 where generated using

$$U_{\theta plate} \approx 4.0 \times 10^{-7}\,\text{J/m} \cdot \frac{1}{\theta_{full} L^2}, \tag{B.4}$$

for specific values of θ_{full} and L, which are labeled in Figure 7A and B. Equation (B.4) was simplified from Equation (B.1) using the following assumptions:

Assumption (1): The relative permittivity, ε_r, was set to one since most MMAs operate in an air or vacuum environment.

Assumption (2): The maximum voltage, V_{max}, was set to 300V since 300V is the largest voltage that could theoretically be applied between two plate actuators made of silicon separated by a vacuum or air-filled gap according to Paschen's law [51]. In practice, however, it is not likely that any MMA could ever operate near such a high voltage value because of the limitations of existing MMA electronics and the fact that the plate actuators are likely to short first due to surface roughness or pull-in failure before the medium between the plates breaks down according to Paschen's law.

Assumption (3): The gap distance between the actuator plates, d_{plate}, was set to the near smallest geometrically feasible value it could be to enable the design's mirror element to rotate over its rotational equilibrium range of motion, θ_{eq}, without causing the plates to collide according to

$$d_{plate} = \theta_{eq} \frac{L}{2}. \tag{B.5}$$

Since the mirror elements of most plate-actuated MMAs can be rotated the same amount in both directions from their passive equilibrium position $\theta_{eq}=\theta_{full}/2$ can be plugged into Equation (B.5).

Assumption (4): The lever ratio, γ_L, was set to be ¼ because, in the best-case scenario, the actuators should occupy as much of the full area underneath the mirror element as possible and they should be spread out as far as possible under the edges of the mirror element. Thus, for typical designs

with square-shaped mirror elements, the shortest distance from the axis of the rotational DOF to the location where the actuators impart their effective point force on the mirror element is close to $L/4$. Although different shaped mirror elements could improve this number slightly, γ_L=¼ is a good assumption for general designs that wisely utilize the full area available below the mirror element for the actuators.

Assumption (5): The actuator-area ratio, γ_A, was set to be ½ because, in the best-case scenario, half of the area available to each mirror system is utilized by actuators to rotate the mirror element about the axis of its rotational DOF. If electrostatic actuators could be bipolar (i.e., they could push and pull on the MMA mirror elements), the entire available area could be utilized to rotate the mirror elements instead of just half of the area.

B.2 Comb Actuators

B.2.1 Performance Limit Equation

The angular energy density limit of general MMA designs that achieve at least tip and tilt DOFs using comb actuators, $U_{\theta comb}$, is defined as

$$U_{\theta comb} = \frac{\varepsilon_r \varepsilon_0 V_{max}^2 \theta_{full}}{4 d_{gap}^2} \cdot \frac{\gamma_L \gamma_A}{\gamma_c}, \tag{B.6}$$

where the parameter, d_{gap}, is the gap distance between the actuators' meshed comb teeth, and γ_c is the comb ratio defined as

$$\gamma_c = \frac{d_{cpitch}}{2d_{gap}}, \tag{B.7}$$

where d_{cpitch} is the pitch of the teeth on each comb (i.e., the distance from the center of one tooth on a comb to the center of its neighboring tooth on the same comb).

B.2.2 Assumptions Used to Simply the Performance Limit Equation

The angular energy density performance limits of comb-actuated MMA designs, $U_{\theta comb}$, plotted as the dashed green lines in Figure 7 where generated using

$$U_{\theta comb} \approx 3.1\times10^3 \text{ J/m}^3 \cdot \theta_{full}. \tag{B.8}$$

Equation (B.8) was simplified from Equation (B.6) using Assumptions (1), (2), (4), and (5) from Section B.1.2 in addition to the following new assumptions:

Assumption (1): The gap distance between the actuators' meshed comb teeth, d_{gap}, was set to 2μm because 2μm is near the smallest gap distance that can currently be fabricated using existing microfabrication technologies. Note also that in the best-case scenario, the meshed teeth of the comb actuators can be aligned such that d_{gap} is independent of how much the mirror element is rotated (i.e., d_{gap} can be independent of θ_{eq}).

Assumption (2): The comb ratio, γ_c, was set to be 2. Note that as the comb teeth become increasingly thin, this ratio approaches a value of 1. Although the smallest values for γ_c are desired to produce the largest $U_{\theta comb}$, it is impossible for the comb teeth to be infinitely thin and if they become too thin, they will lose the stiffness necessary to prevent shorting failure from electrostatic

pull-in. Thus, 2 was selected for this ratio since it corresponds with the smallest practical value that is also typical for most comb-actuated designs that have been optimized to prevent pull-in failure [50]. Note that a design with γ_c=2 possesses comb teeth that are equal in thickness to the gap distance, d_{gap}, between the meshed comb teeth.

B.3 Thermal Actuation

B.3.1 Performance Limit Equation

The angular or translational energy density limit of general MMA designs that achieve at least tip and tilt DOFs using thermal actuators, $U_{thermal}$, is defined as

$$U_{thermal} = \frac{1}{2} E_{thermal} \varepsilon_{Tmax}^2 \gamma_T , \tag{B.9}$$

where $E_{thermal}$ is the Young's modulus of the thermally actuated material, ε_{Tmax} is the maximum strain of the material due to thermal expansion, and the thermal volume ratio, γ_T, is defined as

$$\gamma_T = \frac{V_{thermal}}{L^3} , \tag{B.10}$$

where $V_{thermal}$ is the total volume of the thermally actuated material within each mirror system in the array.

B.3.2 Assumptions Used to Simply the Performance Limit Equation

The angular or translational energy density performance limits of thermal-actuated MMA designs, $U_{thermal}$, plotted as the dashed orange lines in Figure 7 where generated using

$$U_{thermal} = 169.1\left(\mathrm{J/m^3}\right). \tag{B.11}$$

This constant limit was calculated by simplifying Equation (B.9) using the following assumptions:

Assumption (1): The Young's modulus, $E_{thermal}$, was set to 69GPa. This modulus is the Young's modulus of aluminum, which is a typical material choice for MMA thermal actuators because compared to other material options that can be deposited on silicon, aluminum has one of the larger thermal expansion mismatches compared to silicon (i.e., the difference between the thermal expansion coefficient of aluminum and silicon is comparably large).

Assumption (2): The maximum thermal strain, ε_{Tmax}, was set to 0.7% because this strain is the upper limit achieved by aluminum thermal actuators since such actuators will typically fail if they exceed temperature changes of 300K beyond room temperature [54,78–82].

Assumption (3): The thermal volume ratio, γ_T, was set to 1×10^{-4} because this value is on the high end of most existing thermal-actuated MMA designs, which possess thermal ratio values that typically vary between 1×10^{-5} and 1×10^{-4} [54,78–82]. Although this ratio lumps much of the structural complexity of each design into a single term, it was found to be relatively consistent across the thermal MMA designs reviewed.

B.4 Piezo Actuation

B.4.1 Performance Limit Equation

The angular or translational energy density limit of general MMA designs that achieve at least tip and tilt DOFs using piezo actuators, U_{piezo}, is defined as

$$U_{piezo} = \frac{1}{2} E_{piezo} \varepsilon_{PZ\max}^2 \gamma_{PZ}, \tag{B.12}$$

where E_{piezo} is the Young's modulus of the piezoelectric material, ε_{PZmax} is the maximum strain of the material due to the piezoelectric effect, and the piezo volume ratio, γ_{PZ}, is defined as

$$\gamma_{PZ} = \frac{V_{piezo}}{L^3}, \tag{B.13}$$

where V_{piezo} is the total volume of the piezoelectric material within each mirror system in the array.

B.4.2 Assumptions Used to Simply the Performance Limit Equation

The angular or translational energy density performance limits of piezo-actuated MMA designs, U_{piezo}, plotted as the dashed purple lines in Figure 7 where generated using

$$U_{piezo} = 86.0\left(\mathrm{J/m^3}\right). \tag{B.14}$$

This constant limit was calculated by simplifying Equation (B.12) using the following assumptions:

Assumption (1): The Young's modulus, E_{piezo}, was set to 86GPa. This modulus is the Young's modulus of Lead Zirconate Titanate, which is the most commonly used piezoelectric material for MMA piezo actuators [83–87].

Assumption (2): The maximum piezo induced strain, ε_{PZmax}, was set to 0.2% because this strain is the upper limit achieved by Lead Zirconate Titanate piezo actuators since their maximum allowable electric field is 2kV/mm [88,89].

Assumption (3): The piezo volume ratio, γ_{PZ}, was set to 5×10^{-4} because this value is on the high end of most existing piezo-actuated MMA designs, which possess piezo ratio values that typically vary between 1×10^{-5} and 5×10^{-4} [83–87]. Although this ratio lumps much of the structural complexity of each design into a single term, it was found to be relatively consistent across the piezo MMA designs reviewed.

B.5 Lorentz Actuation

B.5.1 Performance Limit Equation

The angular energy density limit of general MMA designs that achieve at least tip and tilt DOFs using Lorentz actuators, $U_{\theta Lorentz}$, is defined as

$$U_{\theta Lorentz} = \frac{B\theta_{full}\gamma_L}{2}\sqrt{\frac{Nhd_{trace}\Delta T}{\rho_\Omega}\cdot\frac{\gamma_A\gamma_S}{\gamma_{trace}}}, \tag{B.15}$$

where B is the magnetic field strength of the actuator magnets, which are typically stationary and located below each mirror element within the array. The parameter N is the number of trace layers, which are typically embedded on or within the array's moving mirror elements and constitute the trace coils through which current is conducted. The convection coefficient, h, is a special

coefficient used to define the heat transfer from the current-heated mirror elements to the air surrounding them. The parameter, d_{trace}, is the depth of each layer of trace coils on or within each mirror element. The parameter, ΔT, is the amount each mirror element increases in temperature from room temperature due to the current flowing through their traces. The parameter, ρ_{Ω}, is the resistivity of the trace material, and γ_S is the system's surface-area ratio defined as

$$\gamma_S = \frac{A_S}{L^2}, \tag{B.16}$$

where A_S is the total surface area of the heated mirror element. The trace ratio, γ_{trace}, in Equation (B.15) is defined as

$$\gamma_{trace} = \frac{d_{tpitch}}{t_{trace}}, \tag{B.17}$$

where d_{tpitch} is the distance between the center of one trace line and the center of its neighboring trace line within the trace coils of each layer (i.e., the pitch of the trace lines). The parameter, t_{trace}, is the thickness of each trace line.

B.5.2 Assumptions Used to Simply the Performance Limit Equation

The angular energy density performance limits of Lorentz-actuated MMA designs, $U_{\theta Lorentz}$, plotted as the dashed blue lines in Figure 7 were generated using

$$U_{\theta Lorentz} = 686.8\left(\mathrm{J/m^3}\right) \cdot \theta_{full}. \tag{B.18}$$

Equation (B.18) was simplified from Equation (B.15) using Assumption (4) from Section B.1.2 in addition to the following new assumptions of this section:

Assumption (1): The magnetic field strength, *B*, was set to 2T since this value is higher than the magnetic field strength achieved by the most powerful natural magnetic material that could be used for Lorentz-actuated MMA designs.

Assumption (2): The number of trace layers, *N*, was set to 2 since it is not currently practical to fabricate more trace layers than one layer on the bottom and another layer on the top surface of each mirror element within the array.

Assumption (3): The convection coefficient, *h*, was conservatively set to an upper limit of $40 W/m^2K$ because experiments suggest that this coefficient is generally below this limit on the microscale [90]. Although at this scale, the main mode of heat transfer is conduction to the surrounding air [90], it can be modeled effectively as convection, so *h* is referred to in this paper as the convection coefficient.

Assumption (4): The trace layer depth, d_{trace}, was set to 10μm because it is currently difficult to deposit layers of trace material deeper than this conservative upper limit.

Assumption (5): The change in temperature, ΔT, of the mirror elements from room temperature caused by flowing current through their embedded trace layers was set to a maximum value of 150K. The reason is that the mirror elements are typically close to their actuation magnets, which should not be heated with a temperature change of 150K beyond room temperature or they will begin to degrade unacceptably and lose their magnetization [91].

Assumption (6): The resistivity of the trace material, ρ_{Ω}, was set to $1.59\times10^{-8}\Omega m$ since this value is the resistivity of silver, which possesses one of the smallest achievable resistivity values found among natural materials.

Assumption (7): The actuator-area ratio, γ_A, was set to 1 because, in the best-case scenario, all of the area available to each mirror system is utilized by actuators to rotate the mirror element about the axis of its rotational DOF. The full area can be used for this purpose because, unlike plate or comb actuators, Lorentz actuators are bipolar and can thus push and pull on each mirror element.

Assumption (8): The surface-area ratio, γ_S, was set to 2 because, in the best-case scenario, each mirror element will occupy the entire area available to each mirror system (i.e., L^2) and each element's total surface area will be approximately twice this area because each element is negligibly thin but possesses two flat sides of equal area.

Assumption (9): The trace ratio, γ_{trace}, was set to 2. Note that the smallest value that this ratio could theoretically be is 1, but that value corresponds to a design where the trace lines within the coils are packed so tightly together that they touch and would thus not function. The chosen ratio of 2 is the smallest practical value that corresponds with a functional design with trace lines that are separated by a gap that is as large as the trace lines are thin. This is reasonable since, for the best case-scenario, the thickness of each trace line and the gap between each trace line should both equal the smallest feature size that could be fabricated.

Bibliography

[1] Valdevit, L., Jacobsen, A. J., Greer, J. R., and Carter, W. B., 2011, "Protocols for the Optimal Design of Multi-Functional Cellular Structures: From Hypersonics to Micro-Architected Materials," J. Am. Ceram. Soc., **94**(SUPPL. 1), pp. 15–34.

[2] Chen, H., Wu, B.-I., and Kong, J. A., 2006, "Review of Electromagnetic Theory in Left-Handed Materials," J. Electromagn. Waves Appl., **20**(15), pp. 2137–2151.

[3] Guenneau, S., Movchan, A., Pétursson, G., and Anantha Ramakrishna, S., 2007, "Acoustic Metamaterials for Sound Focusing and Confinement," New J. Phys., **9**(11), pp. 399–399.

[4] Hopkins, J. B., Song, Y., Lee, H., Fang, N. X., and Spadaccini, C. M., 2016, "Polytope Sector-Based Synthesis and Analysis of Microstructural Architectures With Tunable Thermal Conductivity and Expansion," J. Mech. Des., **138**(5), p. 51401.

[5] Zheng, X., Smith, W., Jackson, J., Moran, B., Cui, H., Chen, D., Ye, J., Fang, N., Rodriguez, N., Weisgraber, T., and Spadaccini, C. M., 2016, "Multiscale Metallic Metamaterials," Nat. Mater., **15**(10), pp. 1100–1106.

[6] Vaezi, M., Chianrabutra, S., Mellor, B., and Yang, S., 2013, "Multiple Material Additive Manufacturing – Part 1: A Review," Virtual Phys. Prototyp., **8**(1), pp. 19–50.

[7] Cecil, J., Bharathi Raj Kumar, M. B., Lu, Y., and Basallali, V., 2016, "A Review of Micro-Devices Assembly Techniques and Technology," Int. J. Adv. Manuf. Technol., **83**(9–12), pp. 1569–1581.

[8] Hopkins, J. B., 2010, "Design of Flexure-Based Motion Stages for Mechatronic Systems via Freedom, Actuation and Constraint Topologies (FACT)," Massachusetts Institute of Technology.

[9] Shelby, R. A., 2001, "Experimental Verification of a Negative Index of Refraction," Science (80-.)., **292**(5514), pp. 77–79.

[10] Smith, D. R., Smith, D. R., Padilla, W. J., Padilla, W. J., Vier, D. C., Vier, D. C., Nemat-Nasser, S. C., Nemat-Nasser, S. C., Schultz, S., and Schultz, S., 2000, "Composite Medium with Simultaneously Negative Permeability and Permittivity," Phys. Rev. Lett., **84**(18), pp. 4184–4187.

[11] Pendry, J. B., Holden, A. J., Robbins, D. J., and Stewart, W. J., 1999, "Magnetism from Conductors and Enhanced Nonlinear Phenomena," IEEE Trans. Microw. Theory Tech., **47**(11), pp. 2075–2084.

[12] Eleftheriades, G. V., and Balmain, K. G., eds., 2005, *Negative-Refraction Metamaterials: Fundamental Principles and Applications*, John Wiley & Sons, Inc., Hoboken, NJ, USA.

[13] Li, J., and Chan, C. T., 2004, "Double-Negative Acoustic Metamaterial," Phys. Rev. E, **70**(5), p. 55602.

[14] Zadpoor, A. A., 2016, "Mechanical Meta-Materials," Mater. Horizons, **3**(5), pp. 371–381.

[15] Grima, J. N., and Caruana-Gauci, R., 2012, "Mechanical Metamaterials: Materials That Push Back," Nat. Mater., **11**(7), pp. 565–566.

[16] Ch, E. A. R., 2014, "Ultralight, Ultrastiff Mechanical Metamaterials," **344**(6190), pp. 1373–1378.

[17] Carneiro, V. H., Meireles, J., and Puga, H., 2013, "Auxetic Materials — A Review," Mater. Sci., **31**(4), pp. 561–571.

[18] Xu, S., Shen, J., Zhou, S., Huang, X., and Xie, Y. M., 2016, "Design of Lattice Structures with Controlled Anisotropy," Mater. Des., **93**, pp. 443–447.

[19] Liu, A. Q., Zhu, W. M., Tsai, D. P., and Zheludev, N. I., 2012, "Micromachined Tunable Metamaterials: A Review," J. Opt. (United Kingdom), **14**(11), p. 114009.

[20] Turpin, J. P., Bossard, J. A., Morgan, K. L., Werner, D. H., and Werner, P. L., 2014, "Reconfigurable and Tunable Metamaterials: A Review of the Theory and Applications," Int. J. Antennas Propag., **2014**, pp. 1–18.

[21] Cummer, S. A., Christensen, J., and Alù, A., 2016, "Controlling Sound with Acoustic Metamaterials," Nat. Rev. Mater., **1**(3), p. 16001.

[22] Baz, A. M., 2010, "An Active Acoustic Metamaterial With Tunable Effective Density," J. Vib. Acoust., **132**(4), p. 41011.

[23] Grima, J. N., Caruana-Gauci, R., Dudek, M. R., Wojciechowski, K. W., and Gatt, R., 2013, "Smart Metamaterials with Tunable Auxetic and Other Properties," Smart Mater. Struct., **22**(8).

[24] Song, Y., Dohm, P. C., Haghpanah, B., Vaziri, A., and Hopkins, J. B., 2016, "An Active Microarchitectured Material That Utilizes Piezo Actuators to Achieve Programmable Properties," Adv. Eng. Mater., **18**(7), pp. 1113–1117.

[25] Chen, H. T., Taylor, A. J., and Yu, N., 2016, "A Review of Metasurfaces: Physics and Applications," Reports Prog. Phys., **79**(7).

[26] Liu, T. L., and Kim, C.-J. C., 2014, "Turning a Surface Superrepellent Even to Completely Wetting Liquids," Science (80-.)., **346**(6213), pp. 1096–1100.

[27] Song, Y., Panas, R. M., and Hopkins, J. B., 2018, "A Review of Micromirror Arrays," Precis. Eng., **51**(August 2017), pp. 729–761.

[28] Shaw, L. A., and Hopkins, J. B., 2015, "An Actively Controlled Shape-Morphing Compliant Microarchitectured Material," J. Mech. Robot., **8**(2), p. 21019.

[29] Barbarino, S., Bilgen, O., Ajaj, R. M., Friswell, M. I., and Inman, D. J., 2011, "A Review of Morphing Aircraft," J. Intell. Mater. Syst. Struct., **22**(9), pp. 823–877.

[30] Yano, M., Yamagishi, F., and Tsuda, T., 2005, "Optical MEMS for Photonic Switching-Compact and Stable Optical Crossconnect Switches for Simple, Fast, and Flexible Wavelength Applications in Recent Photonic Networks," IEEE J. Sel. Top. Quantum Electron., **11**(2), pp. 383–394.

[31] Liao, C., and Tsai, J., 2009, "The Evolution of MEMS Displays," IEEE Trans. Ind. Electron., **56**(4), pp. 1057–1065.

[32] Jung, I. W., Peter, Y.-A., Carr, E., Wang, J.-S., and Solgaard, O., 2007, "Single-Crystal-Silicon Continuous Membrane Deformable Mirror Array for Adaptive Optics in Space-Based Telescopes," IEEE J. Sel. Top. Quantum Electron., **13**(2), pp. 162–167.

[33] Débarre, D., Botcherby, E. J., Watanabe, T., Srinivas, S., Booth, M. J., and Wilson, T., 2009, "Image-Based Adaptive Optics for Two-Photon Microscopy," Opt. Lett., **34**(16), p. 2495.

[34] Doble, N., and Williams, D. R., 2004, "The Application of MEMS Technology for Adaptive Optics in Vision Science," IEEE J. Sel. Top. Quantum Electron., **10**(3), pp. 629–635.

[35] Smith, S. T., 2014, *Flexures: Elements of Elastic Mechanisms*, CRC Press.

[36] Howell, L. L., and Midha, a., 1994, "A Method for the Design of Compliant Mechanisms With Small-Length Flexural Pivots," J. Mech. Des., **116**(1), p. 280.

[37] Bapat, S. G., 2015, "On the Design and Analysis of Compliant Mechanisms Using the Pseudo-

Rigid-Body Model Concept."

[38] Bendsøe, M. P., and Sigmund, O., 2004, *Topology Optimization*, Springer Berlin Heidelberg, Berlin, Heidelberg.

[39] Hopkins, J. B., 2007, "Design of Parallel Flexure Systems via Freedom and Constraint Topologies (FACT)," Massachusetts Institute of Technology.

[40] Hopkins, J. B., 2010, "Design of Flexure-Based Motion Stages for Mechatronic Systems via Freedom, Actuation and Constraint Topologies (FACT)," Massachusetts Institute of Technology.

[41] Hopkins, J. B., 2013, "Designing Hybrid Flexure Systems and Elements Using Freedom and Constraint Topologies," Mech. Sci., **4**(2), pp. 319–331.

[42] Hopkins, J. B., and Culpepper, M. L., 2010, "A Screw Theory Basis for Quantitative and Graphical Design Tools That Define Layout of Actuators to Minimize Parasitic Errors in Parallel Flexure Systems," Precis. Eng., **34**(4), pp. 767–776.

[43] Hopkins, J. B., and Panas, R. M., 2013, "Eliminating Parasitic Error in Dynamically Driven Flexure Systems," Annu. Meet. Am. Soc. Precis. Eng., (C), pp. 1–2.

[44] BARUS, C., 1900, "A Treatise on the Theory of Screws," Science (80-.)., **12**(313), pp. 1001–1003.

[45] Hopkins, J. B., Lange, K. J., and Spadaccini, C. M., 2013, "Designing Microstructural Architectures With Thermally Actuated Properties Using Freedom, Actuation, and Constraint Topologies," J. Mech. Des., **135**(6), p. 61004.

[46] Silex Microsystems, 2017, *MEMS and Sensors Whitepaper Series MEMS Actuators : An Overview of Capabilities , Fabrication Processes , and Materials Selection*.

[47] Madou, M. J., 2011, *Fundamentals of Microfabrication and Nanotechnology*, CRC Press.

[48] Bell, D. J., Lu, T. J., Fleck, N. A., and Spearing, S. M., 2005, "MEMS Actuators and Sensors: Observations on Their Performance and Selection for Purpose," J. Micromechanics Microengineering, **15**(7), pp. S153–S164.

[49] Bifano, T. G., and Stewart, J. B., 2005, "High-Speed Wavefront Control Using MEMS Micromirrors," Opt. Photonics 2005, **5895**, pp. 1–9.

[50] Hopkins, J. B., Panas, R. M., Song, Y., and White, C. D., 2017, "A High-Speed Large-Range Tip-Tilt-Piston Micromirror Array," J. Microelectromechanical Syst., **26**(1), pp. 196–205.

[51] Ono, T., Sim, D. Y., and Esashi, M., 2000, "Micro-Discharge and Electric Breakdown in a Micro-Gap," J. Micromechanics Microengineering, **10**(3), pp. 445–451.

[52] Hopkins, J. B., and McCalib, D., 2016, "Synthesizing Multi-Axis Flexure Systems with Decoupled Actuators," Precis. Eng., **46**, pp. 206–220.

[53] Milanovi, V., Matus, G. A., and Mccormick, D. T., 2004, "Tip-Tilt-Piston Actuators for High Fill-Factor Micromirror Arrays," *Solid-State Sensor, Actuator and Microsystems Workshop*, Hilton Head Island, South Carolina.

[54] Wu, L., Maley, S. B., Dooley, S. R., Nelson, T. R., McManamon, P. F., and Xie, H., 2008, "A Large-Aperture, Piston-Tip-Tilt Micromirror for Optical Phase Array Applications," *2008 IEEE 21st International Conference on Micro Electro Mechanical Systems*, IEEE, Tucson, AZ, pp. 754–757.

[55] Burke, E. K., and Kendall, G., eds., 2005, *Search Methodologies*, Springer US, Boston, MA.

[56] Haimes, Y. V., Lasdon, L. S., and Wismer, D. A., 1971, "On a Bicriterion Formulation of the Problems of Integrated System Identification and System Optimization," IEEE Trans. Syst. Man. Cybern., **SMC-1**(3), pp. 296–297.

[57] Yu, P. L., 1973, "A Class of Solutions for Group Decision Problems," Manage. Sci., **19**(8), pp. 936–946.

[58] Wierzbicki, A. P., 1986, "On the Completeness and Constructiveness of Parametric Characterizations to Vector Optimization Problems," Operations-Research-Spektrum, **8**(2), pp. 73–87.

[59] Wierzbicki, A. P., 1981, "A Mathematical Basis for Satisficing Decision Making," pp. 465–486.

[60] Das, I., and Dennis, J. E., 1998, "Normal-Boundary Intersection: A New Method for Generating the Pareto Surface in Nonlinear Multicriteria Optimization Problems," SIAM J. Optim., **8**(3), pp. 631–657.

[61] Goldberg, D. E., 1989, *Genetic Algorithms in Search, Optimization and Machine Learning*, Addison-Wesley Longman Publishing, Boston, MA, USA.

[62] Fishburn, P. C., 1974, “Exceptional Paper - Lexicographic Orders, Utilities and Decision Rules: A Survey,” Manage. Sci., **20**(11), pp. 1442–1471.

[63] Charnes, A., and Cooper, W. W., 1977, “Goal Programming and Multiple Objective Optimizations,” Eur. J. Oper. Res., **1**(1), pp. 39–54.

[64] Jong, K. A. De, 2006, *Evolutionary Computation: A Unified Approach*, MIT Press.

[65] Padhye, N., Bhardawaj, P., and Deb, K., 2013, “Improving Differential Evolution through a Unified Approach,” J. Glob. Optim., **55**(4), pp. 771–799.

[66] Luo, Z., Chen, L., Yang, J., Zhang, Y., and Abdel-Malek, K., 2005, “Compliant Mechanism Design Using Multi-Objective Topology Optimization Scheme of Continuum Structures,” Struct. Multidiscip. Optim., **30**(2), pp. 142–154.

[67] Bendsøe, M. P., and Sigmund, O., 2004, *Topology Optimization: Theory, Methods, and Applications*, Springer Berlin Heidelberg, Berlin, Heidelberg.

[68] Sigmund, O., 1997, “On the Design of Compliant Mechanisms Using Topology Optimization,” Mech. Struct. Mach., **25**(4), pp. 493–524.

[69] Cao, L., Dolovich, A. T., Schwab, A. L., Herder, J. L., and Zhang, W. (Chris), 2015, “Toward a Unified Design Approach for Both Compliant Mechanisms and Rigid-Body Mechanisms: Module Optimization,” J. Mech. Des., **137**(12), p. 122301.

[70] Fletcher, R., 2000, *Practical Methods of Optimization*, John Wiley & Sons, Ltd, Chichester, West Sussex England.

[71] Gill, P. E., Murray, W., and Wright, M. H., 1981, *Practical Optimization*, Academic Press.

[72] Lewis, R. M., Torczon, V. J., and Kolda, T. G., 2006, *A Generating Set Direct Search Augmented Lagrangian Algorithm for Optimization with a Combination of General and Linear Constraints.*, Albuquerque, NM, and Livermore, CA (United States).

[73] Conn, A. R., Gould, N. I. M., and Toint, P., 1991, “A Globally Convergent Augmented Lagrangian Algorithm for Optimization with General Constraints and Simple Bounds,” SIAM J. Numer. Anal., **28**(2), pp. 545–572.

[74] Conn, A. R., Gould, N., and Toint, P. L., 1997, "A Globally Convergent Lagrangian Barrier Algorithm for Optimization with General Inequality Constraints and Simple Bounds," Math. Comput., **66**(217), pp. 261–289.

[75] Gill, P. E., Murray, W., and Wright, M. H., 1991, *Numerical Linear Algebra and Optimization*, Addison-Wesley.

[76] Cowin, S. C., and Mehrabadi, M. M., 1995, "Anisotropic Symmetries of Linear Elasticity," Appl. Mech. Rev., **48**(5), p. 247.

[77] Okada, Y., and Tokumaru, Y., 1984, "Precise Determination of Lattice Parameter and Thermal Expansion Coefficient of Silicon between 300 and 1500 K," J. Appl. Phys., **56**(2), pp. 314–320.

[78] Wu, L., Dooley, S., Watson, E. A., McManamon, P. F., and Xie, H., 2010, "A Tip-Tilt-Piston Micromirror Array for Optical Phased Array Applications," J. Microelectromechanical Syst., **19**(6), pp. 1450–1461.

[79] Jia, K., Samuelson, S. R., and Xie, H., 2010, "Single-Wafer Solution and Optical Phased Array Application of Micro-Mirror Arrays with High Fill Factor and Large Sub-Apertures," *2010 IEEE 23rd International Conference on Micro Electro Mechanical Systems (MEMS)*, IEEE, pp. 180–183.

[80] Jia, K., Samuelson, S. R., and Xie, H., 2011, "High-Fill-Factor Micromirror Array With Hidden Bimorph Actuators and Tip-Tilt-Piston Capability," J. Microelectromechanical Syst., **20**(3), pp. 573–582.

[81] Jia, K., Pal, S., and Xie, H., 2009, "High-Fill-Factor, Tip-Tilt-Piston Micromirror Array with Hidden Bimorph Actuators and Surface Mounting Capability," *2009 IEEE/LEOS International Conference on Optical MEMS and Nanophotonics*, IEEE, Clearwater, FL, pp. 67–68.

[82] Jia, K., Pal, S., and Xie, H., 2009, "An Electrothermal Tip-Tilt-Piston Micromirror Based on Folded Dual S-Shaped Bimorphs," J. Microelectromechanical Syst., **18**(5), pp. 1004–1015.

[83] Kim, S.-G., Hwang, K.-H., and Koo, M. K., 1999, "Thin-Film Micromirror Array (TMA) for Cost-Competitive Information Display Systems," SID Symp. Dig. Tech. Pap., **30**(1), p. 982.

[84] Yee, Y., Bu, J. U., Ha, M., Choi, J., Oh, H., Lee, S., and Nam, H., 2001, "Fabrication and Characterization of a PZT Actuated Micromirror with Two-Axis Rotational Motion for Free Space Optics," *Technical Digest. MEMS 2001. 14th IEEE International Conference on Micro Electro Mechanical Systems (Cat. No.01CH37090)*, IEEE, pp. 317–320.

[85] Liao, W., Liu, W., Rogers, J. E., Tang, Y., Wang, B. P., and Xie, H., 2013, "A Tip-Tilt-Piston Piezoelectric Scanning Micromirror with Folded PZT Unimorph Actuators," *2013 Transducers & Eurosensors XXVII: The 17th International Conference on Solid-State Sensors, Actuators and Microsystems (TRANSDUCERS & EUROSENSORS XXVII)*, IEEE, Barcelona, pp. 526–529.

[86] Zhu, Y., Liu, W., Jia, K., Liao, W., and Xie, H., 2011, "A Piezoelectric Unimorph Actuator Based Tip-Tilt-Piston Micromirror with High Fill Factor and Small Tilt and Lateral Shift," Sensors Actuators A Phys., **167**(2), pp. 495–501.

[87] Liu, W., Zhu, Y., Jia, K., Liao, W., Tang, Y., Wang, B., and Xie, H., 2013, "A Tip–tilt–piston Micromirror with a Double S-Shaped Unimorph Piezoelectric Actuator," Sensors Actuators A Phys., **193**, pp. 121–128.

[88] Hoffmann, M. J., Hammer, M., Endriss, A., and Lupascu, D. C., 2001, "Correlation between Microstructure, Strain Behavior, and Acoustic Emission of Soft PZT Ceramics," Acta Mater., **49**(7), pp. 1301–1310.

[89] Fan, J., Stoll, W. A., and Lynch, C. S., 1999, "Nonlinear Constitutive Behavior of Soft and Hard PZT: Experiments and Modeling," Acta Mater., **47**(17), pp. 4415–4425.

[90] Hu, X. J., Jain, A., and Goodson, K. E., 2008, "Investigation of the Natural Convection Boundary Condition in Microfabricated Structures," Int. J. Therm. Sci., **47**(7), pp. 820–824.

[91] Arnold, D. P., and Wang, N., 2009, "Permanent Magnets for MEMS," J. Microelectromechanical Syst., **18**(6), pp. 1255–1266.